EOS Encyclopedia of SENSORS
www.aspbs.com/eos

Pulse-Position Type Fluxgate Sensors

Gábor Vértesy

Hungarian Academy of Sciences, Research Institute for Technical Physics and Materials Science, Budapest, Hungary

CONTENTS

1. Overview of Fluxgate Sensors
2. Pulse Position Type Fluxgate Magnetometers
3. Fluxset Sensor
4. Application of Fluxset Sensor
5. Conclusion
   Glossary
   References

1. OVERVIEW OF FLUXGATE SENSORS

Fluxgate sensors measure the absolute strength of a surrounding dc or low-frequency ac magnetic field or the difference in field strength between two different points within a magnetic field. They are vector devices, i.e., sensitive to the field direction. They differ from induction coils, which respond to the time derivative of the magnetic field strength. These sensors are capable for measuring weak magnetic fields. Their measuring range and their resolution are just within the gap between inexpensive sensors such as the magnetoresistive or Hall type sensors and very expensive magnetometers based on quantum effects such as SQUIDs and others.

Fluxgate sensors are solid-state devices without any moving parts and they work in a wide temperature range. They are rugged and reliable and may have low energy consumption. They can reach 10 pT resolution and 1 nT long term stability; 100 pT resolution and 10 nT absolute precision is standard in commercially produced devices. Many dc fluxgate magnetometers have a cutoff frequency of several Hertz, but when necessary, fluxgate can work up to kilohertz frequencies. Fluxgates are temperature stable: The offset drift may be 0.1 nT/°C, and sensitivity tempco is usually around 30 ppm/°C, but some fluxgate magnetometers are compensated up to 1 ppm/°C. Most of the fluxgate sensors work in the feedback mode; the resulting magnetometer linearity is typically 30 ppm.

1.1. Principles of Fluxgate Magnetometers

The detection of the second harmonic component of the sensor output voltage, performed by means of a phase sensitive detector usually preceded by a bandpass filter is the most usual method. The classical description of fluxgate principle is given in [1]. This principle was first used in magnetic modulators. The basic principle is illustrated in Fig. 1. This figure shows the configuration of the most widely used parallel type of fluxgate, for which both the measured and the excitation fields have the same direction. (Another type of fluxgate, not illustrated here, called the orthogonal sensor, has an excitation field perpendicular to the sensitive axis of the sensor, which is identical to the ideal axis of the sensing coil.) The excitation current I_{exc} through the excitation coil produces field that periodically saturates (in both directions) the soft magnetic material of the sensor core. In saturation the permeability drops down and the dc flux associated with the measured dc magnetic field $\boldsymbol{B_0}$ is decreased. The name of the device comes from this "gating" of the flux that occurs when the core is saturated. When the measured field is present, the voltage V_{ind} is induced into the sensing (pick-up) coil at the second (and also higher even) harmonics of the excitation frequency. This voltage, proportional to the measured field, is usually the sensor output. This type of fluxgate magnetometers has a very large literature, it is hopeless to detail them. The most important review articles are given in Section 1.2.

Other methods have also appeared that process the output signal in the time domain. The peak detection method is based on the fact that with increasing measured field, voltage peaks at the sensor output are increasing in one polarity and decreasing simultaneously in the opposite polarity. The difference between the positive and negative peak values is zero for the null field and may be linearly dependent on the measured field within a narrow interval. This procedure gives a stable performance only with core material a magnetization curve of Z-shape and with a sinusoidal premagnetization current. A minimum detectable flux density variation of 0.5 nT was reported in [2]. Further magnetometers based on the pulse-height principle were developed [3, 4] and gave very similar data. The described principle is not applied very often because of stability problems with small fields [5].

ISBN: 1-58883-056-X/$50.00

Encyclopedia of Sensors
Edited by C. A. Grimes, E. C. Dickey, and M. V. Pishko
Volume X: Pages (1–27)

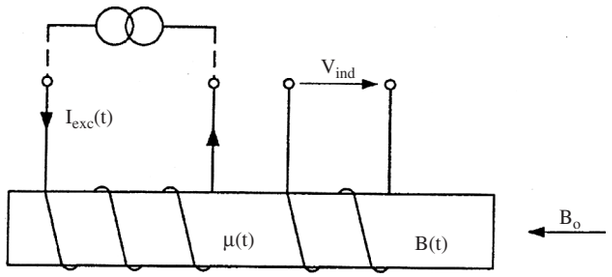

Figure 1. The basic fluxgate principle. The ferromagnetic core is excited by the ac current I_{exc} of frequency f into the excitation winding. The core permeability $\mu(t)$ is therefore changing with $2f$ frequency. If the measured dc field $\boldsymbol{B_0}$ is present, the associated core flux is also changing with $2f$, and voltage V_{ind} is induced in the pickup (measuring) coil (after [33]). Reprinted with permission from [33], P. Ripka, *Sensors and Actuators A* 33, 129 (1992). © 1992, Elsevier.

Probably Marshall constructed the best magnetometer based on this principle in 1971 [6].

Pulse position type fluxgate sensors represent another, more promising type of these devices. The description of these devices, together with their application in a specific area is the main goal of this chapter, so the details will be discussed later.

Auto-oscillation magnetometers are considered as a separate group, although most of them are similar to the previously mentioned ones. The magnetic multivibrator constructed by Takeuchi and Harada [7] consists of a single-core sensor, capacitor and operational amplifier forming the oscillation circuit. The multivibrator duty cycle depends on the amplitude of the measured field. 0.1 nT resolution of this very simple device was reported. A sampling method was used by Son [8]. The instantaneous value of the excitation current at the time of zero-crossing of the core induction depends on the measured field. In an ideal case the sensitivity is not dependent on the excitation frequency, amplitude or waveform. 0.1 nT resolution and 5 μV/nT sensitivity was reached. Sonoda and Ueda used a similar principle in their single-core field sensor [9]. Robertson presented a 1 mm long single-core sensor. Using differential peak detection, a similar sensor excited at 40 MHz had 250 pT/$\sqrt{}$Hz@1 Hz noise [10, 11]. The relaxing-type magnetometer uses a single-core saturated by unipolar pulses and measures the length of the relaxation pulse after the excitation field is switched off. The instrument has $\pm$200 mT range, 5% linearity error and about 0.5 nT p–p noise [12]. Dimitropoulos suggests a new sensor principle combining fluxgate with Mateucci effect [13]. The amorphous 6 cm long wire is excited by flat coil pair. Although the precision of the first prototype is reported to be 60 nT, the device can be scaled down to 5 mm and further optimized. Fluxgate may also work in the short-circuited mode (with current output) [14].

1.2. Historical Overview

The basic principle of fluxgate sensors has been known since the early 1940s, but it was at the beginning of the 1950s that the development stage of these sensors made their technical introduction possible. A comprehensive bibliography of early fluxgate papers was collected by Primdahl [15–17]. The first patent on the fluxgate sensor (in 1931) was credited to Thomas [18]. Aschebrenner and Goubau worked on fluxgate sensors from the late 1920s; by 1936 they reported 0.3 nT resolution on a ring-core sensor [19]. According to Geyger's book [20], they had been working with fluxgate sensors since 1928. Sensitive and stable sensors for submarine detection were developed during World War II. Fluxgate magnetometers were used for space applications. Since Sputnik 3 in 1958, hundreds of fluxgate magnetometers (most of them three-axis) have been launched. Fluxgate magnetometers worked on the Moon [21] and in deep space [22]. Since the 1980s, magnetic variation stations with fluxgate supported by a proton magnetometer [23] have been used for observing changes in the Earth's magnetic field [24].

Later Gordon and Brown [25] and Primdahl [26] wrote review articles on fluxgate sensors. The most important source of information about the development of the fluxgate sensors in Russia and in the former USSR are the books written by Kolachewski [27] and Afanasiev [28]. Japanese fluxgate designs are reviewed in [29]. A lot of information can be found in the VCH monographs on magnetic sensors and among others on fluxgates [30]. A remarkable advanced fluxgate magnetometer was designed for the Oersted satellite launched in 1999 to map the Earth's magnetic field; construction details about that instrument can be found in [31]. The detailed instructions on how to build and calibrate a simple fluxgate magnetometer can be found in [32].

A newer complete review article of fluxgate sensors was published by Ripka [33], where all aspects of these devices are considered. Another work of the same author reviews recent advances and development in the fluxgate technology since the previously mentioned review [34]. Some recent trends are commented in [35]. A broader overview of fluxgates and other magnetic field sensors and magnetometers is made in [36]. Comparative study of uncooled magnetometers and superconducting quantum interference devices (SQUIDs) with proposed hybrid systems can be found in [37].

1.3. Applications

Despite all the efforts on other measuring principles, fluxgate sensors continue to be used in a wide range of applications, because of their high linearity and stability, high direction sensitivity, reliability, riggedness, relative simplicity, and economical operation. Fluxgates have advantages over other types of field sensors in a certain area of measured intensities and frequencies. A general overview of sensors, which are based on soft magnetic materials, can be found in [38]. A lot of valuable information about application of fluxgate sensors are collected in [36] and [39]. Unlike the induction magnetometers, which register field changes only, fluxgate sensors may be used for absolute measurements. Fluxgates also measure the direction of the field, compared with the scalar character of nuclear resonance magnetometers, which are in general better in long-term stability. The fluxgate sensors are more sensitive to the measured field and less sensitive to vibrations and thermal changes compared to optical-fibre magnetometers. Fluxgate

sensors are much cheaper than (more sensitive) SQUIDs and need no liquid helium.

Fluxgate magnetometers are used in geophysics and for space applications. Space applications of fluxgate sensors have been described in references [25, 40, 41], and they were recently reviewed by Acuna [42]. The Giotto experiment [43] and Magsat mission [44] were the most important of the recent fluxgate magnetometer launches.

Three-axis fluxgate magnetometers are widely used for monitoring variations of the Earth's field at magnetic observatories [45, 46], or remote locations [47, 48]. Portable instruments are used for field and airborne measurements of local magnetic field anomalies in mineral prospecting. Applications in archeology are described in [49]. Fluxgate sensors are used for the measurement of rock magnetism [50], as the null sensor in coercivity measurement instruments.

Other applications include sensing of the magnetic ink [51] and magnetic marks on steel ropes [52], location of ferromagnetic bodies [53], detection of submarines and vehicles [54] and missile navigation. Fluxgate sensors are extensively used in compasses for automobiles [55] and aircrafts. The fluxgate principle is also used for indirect measurement of electrical currents in pipelines [56] and in general like current sensors and current comparators [57].

Gradiometric sensors are used in many applications, such as biomagnetic measurement or magnetic testing, where measured field source is in a very short distance. Although single-core fluxgate gradiometer sensor was developed [58], it turned out that for measuring the field gradient using of two separate sensors and subtracting their reading gives better stability of the device. When two top-quality sensors are used, dynamic range of 130 dB for measurements in the Earth's field can be reached. The 50, 000 nT calibration residuals were 2 nT p–p [59, 60].

Magnetic methods of nondestructive evaluation can be used either to monitor material state and properties (such as residual stresses) or to find defects. An overview can be found in [61]. The material properties are tested by using the Barkhausen effect, magnetoacoustic emission, monitoring of the hysteresis loop, and magnetoelastic methods. Material inhomogeneities, cracks, and other defects are monitored by dc methods: magnetic particle inspection and magnetic flux leakage method, or by ac eddy currents. Förster [62] started to use the fluxgate principle for the nondestructive testing of ferromagnetic materials. He is one of the fathers of this method and the author of classic papers. He founded a company that is one of the leading producers of magnetic testing equipments. A first step towards an integrated array of fluxgate sensors is presented in [63]. This chip is believed to arise further possibilities in non-destructive testing applications in the field of soldering tests or current measurements with high area resolution. Other designs are used for special purposes, such as rod-type sensors for non-destructive testing or position testing [64].

Pulse-position type fluxgate sensors are believed to be one of the most promising magnetic sensors in nondestructive material evaluation, especially in eddy current testing. This application will be discussed more detailed later.

Summing up the experience in application, it can be stated, that if resolution in the nanotesla range is required, fluxgates are the best selection. Compared to high-temperature superconducting quantum interference device they may have similar noise level, but the measurement range of fluxgate is much larger. If pT or even smaller fields are measured, a low temperature SQUID should be used. Magnetoresistors, mainly anisotropic magnetoresistance sensors, are the main competitors of fluxgate sensors. Commercially available AMR magnetoresistors have a resolution worse than 10 nT, but they are smaller and cheaper and may consume less energy. Linearity of the best present compensated AMR sensors is 0.05% [65, 66]. It is possible to improve their stability by ac techniques, but the electronics becomes complex and consumes more power. According to the present state of knowledge, if size is not limited, fluxgate sensors are still the winners [67]. The mostly used modern low-noise fluxgate magnetometer is the parallel type with ring core sensor. A phase sensitive detector extracts the second harmonic in the induced voltage, and pick-up coils also serves for the feedback.

1.4. Future Trends

1.4.1. Miniature Fluxgates

One of the possible future developments of fluxgate sensors is their miniaturization, because many applications require very small sensor size. However, the process of the fluxgate sensor miniaturization is complicated, because the magnetic noise dramatically increases with decreasing sensor length. Small-size fluxgate sensors are made of open or closed cores from amorphous material or permalloy and have simple electronics [68]. Up to now, the quality of sputtered or electrodeposited permalloy has not been sufficient for low-noise fluxgate applications, so patterns etched of amorphous tape are often used for the sensor core. Integrated fluxgate sensors do not have wound coils and therefore they can be very small and cheap. Their core is made by sputtering or electrodeposition [69–71]. For low-noise integrated sensors, the cores of amorphous tape are used, as they have better magnetic properties [72].

The compensation sensor, manufactured by Siemens-VAC Hanau (Germany), which has a permalloy wire core may also work as a single-core fluxgate sensor [73]. A number of simple multivibrator-type fluxgate magnetometers were reported from Japan. A 15 mm long hairpin sensor was made up of a strip with helical anisotropy [74]. This classical sensor has 5 nT/$\sqrt{}$Hz noise. The simple "PCB" construction of the 15 mm long fluxgates is described in [75]. The annealed core made of amorphous foil is sandwiched inside multilayer printed circuit board. Outer metal layers of PCB connected by vias form the winding. Resistance of the winding can be decreased by Cu-electroplating after patterning of the winding [76].

Planar fluxgate sensor with flat coils was described in [77], and a similar sensor having three flat excitation coils was shown in [78]. Further improvement was achieved with similar sensor having two layers of ferromagnetic core [70, 71]. Orthogonal fluxgate with flat excitation and pick-up coil was described in [72]. The sensor resolution is 40 nT and the linearity error in the 400 mT range is 0.5%. A parallel mode two axis integrated fluxgate magnetometer by the same authors was developed for a low-power watch compass [72, 79].

Solenoid coils have much better efficiency than flat coils, as they are ideally coupled with the core. However, micromachining of solenoids is difficult. Early devices were developed by Kawahito [80] and Gottfried [81]. The technology was further devoloped by Liakopoulos and Ahn [82, 83]. UV-LIGA based thick photoresist process was used to create electroplated permalloy core and copper coils [84]. New, fully integrated 2D micro-fluxgate magnetometer is described in [85] and in [86]. The magnetometer is integrated in a standard CMOS process and uses a ferromagnetic core integrated on the chip by a photolithographic post-process compatible with the integrated circuit technology. The cross-shaped ferromagnetic core is placed diagonally above four excitation coils, two for each measurement axis. A novel electronic signal extraction technique is presented. The integrated 2D magnetometer exhibits a sensitivity of 160 V/T and a linear range of $\pm 50\ \mu$T. The magnetic equivalent noise spectral density is 70 nT/$\sqrt{\text{Hz}}$ at 1 Hz, and the total power consumption is as low as 17 mW for the 5 V power supply. An integrated array of fluxgate sensors is described in [63].

The microfluxgate technology is improving, but at present AMR sensors have better parameters than fluxgates smaller than 5 mm.

1.4.2. Digital Magnetometers

One of the possible future trends in the development of fluxgate magnetometers is their digitalization. The advantage of using the digital detection is that the reference signal may have arbitrary shape so that it can perfectly match the measured signal—even better that the variable-width detector of the switching type. The present state of art of this problem is reviewed by Ripka [35, 36].

Fully digital fluxgate magnetometer performs the analog-to-digital conversion of the sensor output signal right after the pre-amplification and eventual analog pre-filtering to suppress the unwanted signals. The feasibility of digital signal processing of the fluxgate output was shown in [87]. First real-time fluxgate magnetometer was built in Max-Planck Institute [88].

The harmonic distorsion in the ADC would cause false signal output. As the feedthrough changes with temperature, this effect could degrade the offset stability. The phase-sensitive detection and further filtration is performed numerically in Digital Signal Processor (DSP). Digital fluxgate magnetometer was on board of Astrid-2 satellite [89]. Its power consumption was 2 W, which is still about double than that of similar analog-feedback magnetometer [31]. The weak point of the instrument was the audio DAC which had high offset, offset drift and non-linearity. The instrument noise was about 5 times higher than the sensor noise. Another approach was suggested by Kawahito et al. [90, 91]. They used analog switching-type synchronous detector followed by analog integrator and 2nd order $\Delta\Sigma$ modulator.

The feedback of the digital magnetometers should include voltage-to-current converter to eliminate the influence of the changing resistance of the feedback winding. It should be noted that the increased noise level of the instruments is not the property of digital processing, but it is due to the design compromises to lower the power consumption of the magnetometer electronics: digital laboratory lock-in amplifiers such as SR 830 have very low noise so that they can be used for testing of high performance fluxgate sensors.

2. PULSE POSITION TYPE FLUXGATE MAGNETOMETERS

2.1. Principle of Operation

In spite of the fact, that second harmonic fluxgates are the most frequently used types, the pulse position (or phase-delay) type sensors recently have been intensively developed, and they have found their appropriate field of application. This is a magnetometer with direct encoding of magnetic fields [92, 93]. The particular advantage of this magnetometer is an output signal that can be simply converted into a binary signal, which can be understood by microprocessors. This measurement principle is directly compatible with requirements for digital signal evaluation. This is why the magnetometer can be described as an intelligent sensor when it is combined with a microprocessor. Further advantages of this fluxgate magnetometer are: high linearity, so no feed-back is required; simplicity of manufacture; ruggedness; small dimensions; great sensitivity with adequate stability; low cost due to high integration possibility using high integrated digital circuits as gate arrays.

Figure 2 illustrates the principle of operation of this method. A simple magnetization characteristics is assumed without hysteresis and a triangle waveform of the excitation current is applied. For the time intervals t_1 and t_2 between two succeeding output voltage pulses, the following expressions can be written:

$$t_1 = T/2 - 2\Delta t = T/2 - TH_o/H_m \tag{1}$$

$$t_2 = T/2 + 2\Delta t = T/2 + TH_o/H_m \tag{2}$$

where T is the period of the excitation current, H_m is the excitation field maximum value, and H_o is the measured field.

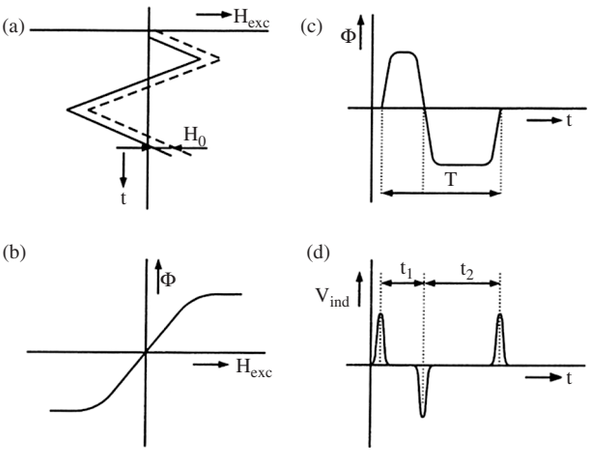

Figure 2. Principle of operation of pulse-position type fluxgate magnetometers: (a) excitation field with dc shift by measured field H_o; (b) magnetization characteristics of the core; (c) flux; and (d) and induced voltage (after [33]). Reprinted with permission from [33], P. Ripka, *Sensors and Actuators A* 33, 129 (1992). © 1992, Elsevier.

Those relations were used by Heinecke in a digital magnetometer, described in [94]. The time intervals t_1 and t_2 were measured by a counter with the reference frequency n times higher than the excitation oscillator frequency. If the time $(t_2 - t_1)$ is equal to N periods of he reference oscillator, then we can write

$$t_2 - t_1 = 2TH_o/H_m = NT/n \tag{3}$$

$$H_o = H_m N/2n \tag{4}$$

The resolution of this method is limited by the maximum counter frequency. A 2.5 nT resolution was reached with a 10 MHz basic oscillator [94]. The resolution was improved to 0.1 nT by summing 100 time intervals, but that caused a significant limitation of the sensor's dynamic response, because the excitation frequency was only 400 Hz. The complications with noise from fast digital signals of the counter and other drawbacks limit the performance of the magnetometers based on this method. A magnetometer working on a similar principle but with analog output is described in [95]. A Heinecke-type magnetometer with a H-core sensor design had a resolution of 10 nT, but the stability of such a sensor is questionable due to an expected large perming effect [96].

2.2. Sensitivity

The sensitivity S is the difference ratio of a change in the output signal to the respective change in the input signal, which is the value to be measured:

$$S = \frac{\Delta_{\text{Output}}}{\Delta_{\text{Input}}} \tag{5}$$

If the differential ratio is used instead, Eq. (5) has to be derived with respect to the measured value H_{ext}. Thus the sensitivity of this type of magnetometer becomes:

$$S = \frac{d(\Delta t)}{dH_{\text{ext}}} = \frac{T}{2H_{\text{ref max}}}, \tag{6}$$

where H_{ref} is the amplitude of the reference field and T is the period of excitation. This expression can be written [30] in the form of:

$$S = \frac{\mu_0 \mu_d \pi T}{4k_2[1 + N(\mu_d - 1)]B_{\text{sat}} h_{\text{ref max}}}, \tag{7}$$

where B_{sat} is the saturation density, μ_d is the relative differential permeability at $B = 0$ on the magnetization curve and k_2 is constant. It is possible to simplify this equation, due to the fact that for common probe core materials and common probe shapes the following two relations can be used:

$$N \gg \frac{1}{\mu_d - 1} \tag{8}$$

and

$$\mu_d \gg 1. \tag{9}$$

Then the sensitivity becomes:

$$S \approx \frac{\pi \mu_0 T}{4k_2 N B_{\text{sat}} h_{\text{ref max}}} \tag{10}$$

This result is important and interesting, because it shows that the sensitivity of the probe is independent of the relative permeability. Thus slight mechanical stress on the probe core or temperature changes, which could effect a change in the relative permeability, do not have any influence on the sensitivity of the probe. Nevertheless, mechanical stress of the probe have to be avoided as they result in an increase of the probe noise.

3. FLUXSET SENSOR

A new version of pulse position type fluxgate sensors, which is named as Fluxset sensor, has been developed recently for measuring dc and ac (up to 200 kHz frequency) low level magnetic fields with high accuracy and stability [97]. The probes are suitable for axial measurement of the magnetic field. The transverse sensitivity is negligible. The device has small size, it is versatile, inexpensive and sufficiently robust to meet the demands of the industry. In the following this sensor will be described more detailed, and some specific applications of the Fluxset sensor in the area of nondestructive material evaluation will be demonstrated.

3.1. Construction of Fluxset Sensor

The probe of the sensor (the measuring head itself) is made of two solenoids wound on each other. The inner and outer solenoids are called driving and pick-up solenoids, respectively. Elliptical shape driving coil was applied in order to decrease the air gap between the core and the coil. The pick-up coil is located outside of the driving coil. The geometry of the probe is shown in Fig. 3. The driving coil has 50–200 turns in single layer with 8–17 mm length (made of isolated copper wire with 0.07 mm diameter), the pick-up coil has 30–100 turns in two layers with 5–20 mm length (made of isolated copper wire with 0.05 mm diameter).

The sensing element of the probe is an amorphous alloy ribbon with high initial permeability and low saturation. This core is periodically saturated by triangle shape magnetic field produced by the current in the driving coil (see Fig. 4). The signal of the pick-up coil (shown also in Fig. 4) is transformed into pulses, the edge of which controls the counting of clock rate. As outlined above, without an external field

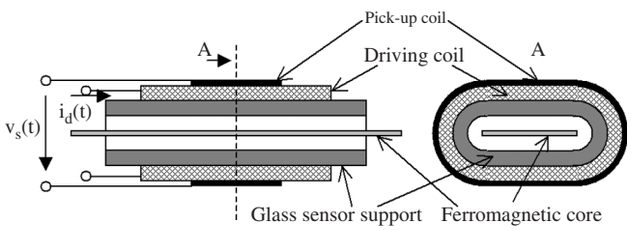

Figure 3. The geometry of Fluxset sensor. Reprinted with permission from [139], J. Pávó, et al., *Sensors and Actuators A* 110, 105 (2004). © 2004, Elsevier.

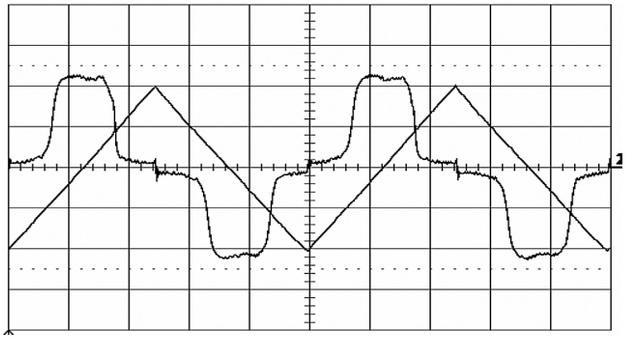

Figure 4. Oscilloscope plot of the current of driving coil (triangle) and the voltage induced in the pick-up coil with zero external field at 10 kHz frequency. (X axis: 20 μsec/div, Y axis: 2 V/div). Reprinted with permission from [97], G. Vértesy, et al., *Sensors and Actuators A*, 85, 202 (2000). © 2000, Elsevier.

the time intervals between pulses are equal. In an external field the magnetization cycle of the core is shifted, and the time intervals between pulses, corresponding to the parallel and anti parallel saturation will be no longer symmetrical. Any distortion in the local magnetic field caused by the soft magnetic core is eliminated by the symmetry of its hysteresis loop.

The sensor was driven by rectangular shaped current signal produced by 6 V amplitude voltage signal from a function generator and the serial linked 1 kOhm resistor. The measured magnetic field was generated by calibrated exciting solenoid was driven by function generator. The pick-up signal was detected and pre-processed by lock-in amplifier. The block diagram of electronics is shown in Fig. 5.

3.2. Numerical Validation of the Sensor

To investigate the behavior of the sensor, different models were used, all of them giving useful and important results. For the simplest sensor model (1D), a theory was developed based on the assumption that the magnetic field components orthogonal of the sensor's axis are neglected. Expressions for the sensor output voltage, sensitivity, measurement range and voltage pulse delay were obtained assuming either piece-wise linear magnetic characteristics or smooth magnetic characteristics for the ribbon core. Based on the results

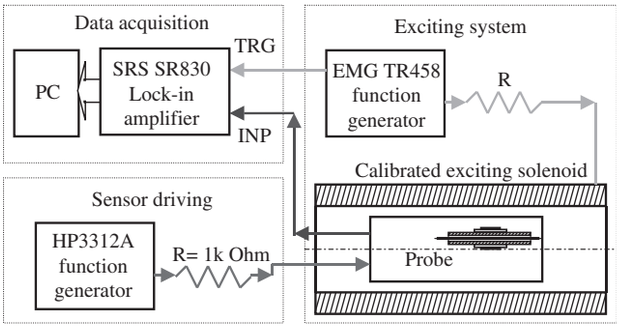

Figure 5. Block diagram of the experimental set-up. Reprinted with permission from [97], G. Vértesy, et al., *Sensors and Actuators A* 85, 202 (2000). © 2000, Elsevier.

recommendations were drawn for the electronic circuit specification and for B–H characteristic extraction procedure. The 1D model was found to be very efficient in the understanding of the sensor's behavior.

For the modeling purposes, the core was considered as an equivalent cylinder with the same cross sectional area [98, 99]. In this way the field problem became a 2D (axisymmetric) one. The solution of the problem was obtained by an original method [98] (the linear PDE for the magnetic vector potential was solved by the separation of variables method and the non-linear boundary conditions, which represents the core was solved by a suitable numerical method, of Katzenelson type). Based on this model, a computer program was developed. It was used to simulate the sensor to obtain its characteristics and to compute the relative sensitivities to design parameters.

The most accurate models developed for the sensor are the 3D non-linear ones. Several techniques were used. The first one is based on Finite Element Method (FEM) [100], the second one on the Integral Equation Method (IEM) [98, 99, 101]. To investigate the behavior of the sensor, a three-dimensional finite element mesh consisting of 4,959 second order hexahedral elements with 22,428 nodes was generated to model one eighth of the core and the driving solenoid. A linear analysis taking into account of the eddy currents in the core was first compared with a static one using the initial permeability of the ferromagnetic material. These showed that the eddy currents in the ribbon had no effect on the field, so a static analysis was sufficient. A reduced magnetic scalar potential formulation with the source field of the coil modeled by edge elements was used. The reference design of the sensor was also analyzed using a 3D nonlinear integral formulation [98, 99, 101]. In the 3D analysis, a Picard-Banach iterative algorithm (whose convergence is theoretically guaranteed) was used to treat the nonlinear magnetic constitutive relationship. The calculation of the output signal of a Fluxset sensor placed in a homogeneous magnetic field based on rigorous numerical modeling of the operation of the sensor has been performed showing a good agreement either with numerical simulation performed by other teams or with the available experimental data. In addition, in the magnetostatic limit, an axisymmetric model though not giving accurate results in terms of the output amplitude signals, was able to predict with a reasonable accuracy the zero crossing points of the output signal which are directly linked with the external field amplitude.

3.3. Analysis of the Sensor's Properties

3.3.1. Spatial Resolution, Linearity and Directional Selectivity

The behavior of the sensor was investigated both by numerical simulations and by experiments. The spatial resolution of a 10 mm length sensor was tested in an inhomogeneous magnetic field environment, by a bobbin coil arrangement, and the spatial resolution of the sensor was found to be in the order of 0.1 mm.

The linearity was determined by numerical simulation [102]. In order to investigate the linearity of the sensor, a finite element model of the core and of the driving solenoid

was developed. The external field oriented in the axial direction was modeled by placing a large solenoid around the arrangement with its current adjusted to yield the desired value of the field in free space. The flux of the pick-up coil was calculated by integrating the magnetic flux density over several cross-sections and the average value was multiplied by the number of turns. Sweeping the range of the driving current within a quarter of the period, the time derivative of the flux was calculated to yield the induced voltage. The external field was assigned several values in the range of 0.5 to 200 μT. The time shift of the voltage impulse at high values of the external field was easily recognizable, but it turned out to be very difficult to determine the time shift if the external field was low. Therefore, the difference of the time integrals of the voltage in the ranges of 50 to 75 μs (negative values of the exciting current) and of 75 to 100 μs (positive values of the exciting current) was chosen as a measure of the time shift instead. This value depends on the flux at the negative maximum of the current, at zero exciting current and at the positive maximum of the current only The dependence of the flux difference on the external field revealed an excellent linearity. This is in good agreement with the experimental results, where the linearity was determined to be better than 1%, being independent of the applied driving frequency.

The directional selectivity of the sensor (the sensitivity of the Fluxset to a magnetic field orthogonal to the ribbon axis) was tested by several measurements and it was also calculated. Some finite element models of the Fluxset sensor were developed and compared. The models are of varying degrees of complexity and can take into account magnetic non-linearities of the amorphous core of the sensor. The developed models were compared and discussed in [103]. In order to find out whether the Fluxset would measure only the axial component of field, or whether it would be affected by transverse components of the field, the device was modeled while placed in an external magnetic field at various angles to the axis of the device. The results would imply that the device measures the component of field, which is parallel to its axis. Studying the behavior in fields with non-zero gradients, it was also found that (at least for uniform gradients) the sensor measures the average field. The effect of transverse fields was also measured. A pancake coil was applied in conjunction with Fluxset. Using a current (and hence a field) which is even higher than the experimental one, the voltage trace is rather distorted, but the measurement is not dramatically affected (less than 2%). The direct measurement of the crossfield effect is difficult, because of the lack of very precise orientation of the fields with respect to the sensor axis. Instead of this, the deviation from the linearity was measured in the presence of orthogonal field, which is a good characteristic of the directional sensitivity. The deviation was found to be of the order of 1%, which is similar to the property of best fluxgate magnetometers.

3.3.2. Time Dependent Behavior, Effect of Eddy Currents in the Sensor Core

The impact of the eddy currents induced in the core of the Fluxset probe was investigated [104–107]. Due to the conductivity of the magnetic core, at high frequencies the skin effect may in fact delay the penetration of the flux generated by the driving solenoid, with a consequent alteration of the output signal. For the unsaturated material the skin depth for the fundamental harmonic of the triangular current waveform spanned from 21 μm at 66.7 kHz to 0.39 mm at 200 Hz, and the critical value $\delta = h/2$ was found to correspond to a frequency of about 35 kHz and a penetration time of 30 μs. Nevertheless, numerical experiments found the growth-time of the magnetic flux to be 3–4 orders of magnitude faster. The explanation of this phenomenon, which occurs in both linear and non-linear cases, was given in [104]. It was outlined here, that two different time scales characterized the diffusion process. While the flux reaches the final value after a few tens of ns, the flux density is at that time far away from its uniform distribution. Field and fluxes can have very different time constants, due to the magnetic nature of the slab and to its finite height. The penetration time of the magnetic flux into the ferromagnetic core of the probe was determined using analytical and numerical calculations. In the non-linear case it was found about 5 ns, that almost coincides with the penetration time of the magnetic field.

The numerical analysis was also carried out using a 3D finite element differential and integral formulation. The numerical integral formulation solves the integral equations in the conducting and in the ferromagnetic domain, in terms of the sources of the magnetic field, namely the current density, expressed in terms of edge element shape functions, and magnetization vector, assumed to be uniform in each finite element within the iron. In spite of a small number of finite elements along the thickness, the penetration time has been found in excellent agreement with the approximate analytical value $t_{sat} = 5.2$ ns. In the linear case, corresponding to small exciting currents, the time scale for the field penetration is about 0.2 μs, but the magnetic flux rise is much faster. The explanation is related to the magnetic nature of the slab and to its finite height. Consequently, it was found that the eddy current effects can then be neglected in the range of frequencies from DC to about 100 MHz. Therefore, a magnetostatic model is acceptable for the characterization of the sensor at its terminals.

3.3.3. Network Model of the Sensor, Investigation and Design of the Overall Performance

Non-linear circuit modeling the operation of the entire Fluxset sensor was developed and tested by comparing the simulated output with the measured one [108, 109]. The network consists of three sub-circuits interconnected by means of controlled sources: one for the driving coil, one for the pick-up coil and the third one for the magnetic circuit. This model takes into account several types of parasitic field effects, such as, eddy currents in the ribbon core, widening of the hysteresis loop, capacitive effects between the windings, etc. Parameters of the circuit model are determined by the results of the rigorous electromagnetic field modeling of the sensor (e.g., results of the calculations mentioned above can be used for the purpose) or by the analysis of experimental results. Details concerning the parameter extraction procedure are presented in [110] and [111]. The non-linear circuit is analyzed using the SPICE network analysis package.

The developed circuit model allows both the analysis of the sensor behavior in a broad frequency band (including computation of the sensor's sensitivity) and the evaluation of the frequency bandwidth for an imposed measurement error. Since the circuit parameters are depending on the physical parameters of the sensor, the circuit model together with the parameter extraction procedure can be effectively used for the optimization of the sensor.

3.3.4. Calibration of the Sensor

The case of a uniform field B_{ext} directed along the ribbon axis was simulated [112, 113] computing the resulting time shift ΔD, as defined in [112]. The ratio $k_{num} = B_{ext}/\Delta D$ is the numerical Fluxset calibration constant, which is in very good agreement (around 2%) with the experimentally measured calibration constant.

The effects of non-uniform fields, moving Fluxset along the axis of some Helmoltz coil pairs, were also investigated. First one coil pair was used. These results showed that if we assume that Fluxset measures the average of the magnetic field, the calibration constant is suitable also for this non-uniform field. In this case there is a very strong correlation between the average field and the field at the center. This means that using another calibration constant it is possible to get a very good agreement between the measured field and the field at the center as well. A further simulation was performed as well with three coil pairs, so that the magnetic field variations are on a spatial scale smaller than the dimensions of Fluxset. In this case, the average field and the field at the center of the core are not correlated. For strongly non-uniform fields Fluxset can be assumed to measure a weighted average of the magnetic field in the region of the core.

Based on the Fluxset sensor model, the measurement chain was simulated and a general software package was developed. This package is able to simulate the output voltage of the sensor and of the measurement chain, starting from the geometrical data and external magnetic field. This package was extremely useful to check the new designs of the sensor. It takes into consideration all essential effects, such as: non-linear B–H characteristic of the ribbon; hysteresis effects in the ribbon; eddy current in the ribbon; capacitive effects between coils. In order to improve the performance of the measurement chain, some further improvements can be done, such as: the use of differential techniques in order to improve the sensor's sensitivity; the use of sigma-delta feedback in order to control in the accurate manner the measurement chain.

3.4. Design of the Sensor Core

3.4.1. Material Choosing and Processing

For the best operation of the device, the material of the sensing element should be chosen very carefully. It is difficult to discuss the selection of the core material generally, because it depends on the type and the geometry of the sensor, on type of processing of the output signal, and also on the excitation frequency and required temperature range. However, there are general requirements for the material properties, which are the following: high initial permeability, low coercivity, low magnetostriction, low Barkhausen noise, low number of structural imperfections, smooth surface, uniform cross section and large homogeneity of parameters, low saturation magnetization and high electrical resistivity. All known studies of core material composition and processing parameters have shown that the minimum noise is achieved for near-zero magnetostriction alloys. References [1, 26, 114] discuss the sensor core material properties.

Amorphous magnetic alloys, which are produced by rapid quenching, represent an excellent type of soft magnetic materials, and they are very suitable for the core material of fluxgate magnetometers. Manufacturing techniques and properties of amorphous magnets are well known for a long time and a number of monographs devoted to these aspects have been published (see, e.g., [115–117]). They started to be used for fluxgate cores from the early 1980s. Properties of these alloys as sensor materials are discussed in [118]. A study concerning the noise of the amorphous magnetic materials was performed in [119]. For Fluxset sensor 0.6 mm wide amorphous alloy ribbon core was prepared by the melt spinning method. The chemical composition, $Fe_7Co_{53}Ni_{17}Cr_3Si_5B_{15}$, was chosen to provide the lowest magnetostriction.

The amplification, the sensitivity and the signal-to-noise ratio of the Fluxset sensor highly depend on the shape and on the slew rate of the induced pulses in the pick-up coil. The influence of the processing of the core material on the operation of the device was investigated [120]. It was found that the proper heat treatment, which followed the mechanical surface polishing improved both the sensitivity and signal/noise ratio. In another work the polishing process was improved by applying new, chemical and electrochemical methods, and interpretation of the effect of polishing on the device's sensitivity was given [121]. The influence of chemical etching was also studied in [122].

The modification of the core material is characterized the best by the signal of the pick-up coil. The largest improvement was achieved by chemical etching. This method yields good homogeneity over the ribbon surface, it can be well controlled, it gives reproducible result in repeated treatments, and it gives the best sensitivity of the device.

For the interpretation of the processing, different effects should be taken into account. The reduction (by about 25%) of the *magnetic cross section* (volume effect) of the core decreases the magnetic field, by which the core can be saturated, contributing such a way to the increase of sensitivity, because the pulses of the pick-up coil become narrower. However, the improvement of the sensitivity, as a function of the removed layer of the surface has a maximum, further decrease of the thickness starts to spoil the device characteristic. This can be attributed to the appearance of new surface inhomogeneities after a long etching. All types of the surface polishing also significantly improved the *surface smoothness*. Any surface roughness contributes to the coercivity [123], this is the reason why the polishing decreases the coercivity, and increases the mobility of the domain walls in the material. This phenomenon can be seen by the lowering of the saturating field in dynamical hysteresis measurement, which leads to the narrowing of the pick-up coil signal. The static hysteresis measurements don't reveal this modification, because in the static saturation-to-saturation hysteresis

curve mainly the domain wall nucleation processes are dominant. Electron probe microanalysis, performed on the air side of the ribbons, before and after polishing, revealed a slight *change in the chemical composition* of the surface; the ratio of Co decreased by about 0.5%, and ratio of Ni and Si increased by about 0.2% after polishing, compared with the original, as-quenched surface. This can be attributed to the removing of the chemically different surface layer. During the quenching a composition gradient can rise in the ribbon, which was indicated by the electron probe microanalysis. The slightly different chemical composition, mainly the different Co content, leads to different magnetic properties. Such a way the magnetic behavior can be improved to make the ribbon more homogeneous by removing the surface layer. Theoretical calculations of the eddy current effect in the core showed [104] that during the fast magnetization of the ribbon, the *magnetic flux density* is larger in the surface region that in the inner part of the material. The magnetic flux penetration has the time-constant in the range of some hundred ns, depending on the actual phase of the magnetization. The flux-penetration effect becomes important only above 100 MHz magnetization frequency. Nevertheless this effect has strong influence on the phase detection of the pick-up signal, which limits the sensitivity of the device. This shows the important role of the surface during the periodic magnetization of the core, and explains why the magnetic behavior of the core becomes better by improving the homogeneity of the surface region. Most probably, the joint effect of different contributions is responsible for the observed improvement of the sensitivity. The different, analyzed effects can not be separated, because any kind of polishing has simultaneous influence on the surface quality, on the volume and on the gradient of the chemical composition, too. Another, important result was also achieved by the surface treatment, the significant increase of the operation frequency of the device. The frequency of the driving current was increased from 100 kHz to 200 kHz, which allows an operation frequency of the device over 100 kHz. This is very important in different applications of the device, mainly in the eddy current nondestructive testing of materials (see later).

3.4.2. Extracting the Magnetic Parameters

The B–H characteristic extraction, using non-uniform field devices is anything but straightforward. This problem is an inverse one and it is important from a theoretical point of view. The approach proposed for extracting the B–H characteristic from external measurement in non-uniform field, by solving the inverse problem is considered an important original contribution by the scientific community [124–126]. Usually, the B–H curve is obtained via an appropriate scaling of the flux-current experimental data, assuming a uniformly distributed magnetic field inside the specimen. This is not the case of the magnetic core of the Fluxset sensor. Therefore, an inversion procedure for this more realistic situation, where magnetic induction, magnetic field and magnetization vectors are space dependent was discussed. In particular, the problem of the uniqueness of the solution of the inverse problem and of the computation of the numerical errors due to the inversion procedure were addressed. For what concerns the first problem, it was shown that the relationship between the relative permeability and the measured mutual inductance M of the system (the slope of the linear flux-current φ-i characteristic), is a continuous increasing function. With reference to the second problem it was shown that, by using complementary formulations, upper and lower bounds for the reluctance of the system can be found as functions of the relative permeability. These bounds give also the confidence interval on the estimate of the relative permeability.

3.4.3. Shape Design of the Core

The shape design of the core is also an important task. From the operational principle of the Fluxset sensor it is obvious that the shape of the output signal has an impact on the sensitivity of the sensor, that is, in addition to the chemical and thermal treatment of the core material, the shape of the core also affects the output signal. It was assumed that the more homogeneous the magnetization of the core material, the better the sensitivity of the sensor. Numerical analysis and an optimization method were developed that were used to find the optimal core shape for a given exciting field. As a result it was concluded, that an elliptical-like shape would provide the best output signal. However, from the calculations we also concluded that the difficulty of manufacturing the complicated shape was not worth the small gain due to the slightly better signal shape. At the same time, from other experiments and parallel calculations, it was found that the length of the core has a larger impact on the signal shape (see next point). Finally it was concluded that the conventional rectangular core shape was more suitable by taking into account all aspects of sensor manufacturing and application.

3.4.4. Optimization of the Size of the Core

The size of the probe core has a large effect on the sensitivity of the device, too. Different numerical models of the sensor core based on electromagnetic field calculation were applied. The results of these simulations were tested by the comparison of the calculated relative sensitivities with the measured ones [127]. The sensitivity means two different things at the same time: the amplification of the device and the level of the noise. In the above-mentioned work the amplification of the sensor was investigated. The simple geometry of the device makes relatively easy the numerical simulation of the sensor.

Three different numerical models based on electromagnetic field calculation were investigated. The relative change of the sensitivity is shown in Table 1, using the results of these three models. The relative sensitivity (S) means the modification of the sensitivity due to the change of the investigated sensor parameter. The three applied models were the following: 3D FEM model [100, 102] for S^1; Axisymmetric (2.5D) analytical model [100] for S^2 and Integral equation model (3D) [98, 128] for S^3.

As it is seen in Table 1, the most deterministic parameter seems to be the length of the ferromagnetic core, because each model predicts a significant increase of sensitivity by increasing the core length. The influence of other parameters is much less, and the scatter of values, by comparing

Table 1. The calculated S relative sensitivities. Reprinted with permission from [127], G. Vértesy and A. Gasparics, *J. Electrical Engineering* 53, 53 (2002). © 2002, Slovak University of Technology.

Parameter	S^1 [%]	S^2 [%]	S^3 [%]
Pick-up coil length	−14	−12.66	−13.72
Driving coil length	−157	0	32.97
Solenoid diameter	2	18.3	10.92
Relative permeability	28	1.62	1.59
Core length	280	147.87	131.79
Core width	7	—	—
Core thickness	37	—	—

different models is also large. Because of this, in the experiments the attention was focused to the study of the core length.

The Fluxset sensor converts the value of the measured magnetic field to the time-shift of the induced voltage pulses in the pick-up coil. The amplification means the ratio between this time shift and the measured magnetic field.

The core material and its geometric parameters (core width and thickness) were also fixed during the experiments. Only the influence of the core length was investigated and the experimental results were compared with the numerical ones. As discussed above, the results of the calculations show that the core length has a strong, positive influence on the sensitivity (Table 1). The experimental results show two different reasons of this phenomenon. These are: (i) the modification of the saturation field, which means that lower value of driving field can be applied, which improves the sensitivity and (ii) the sensitivity also increases by increasing the core length, even the driving field is kept fixed.

Six millimeters length driving coil was applied in the measurements, and three, different length core was used. It can be observed well (Fig. 6), that the longer the core is, the lower driving field is necessary to saturate it, because the width of the induced voltage pulses is narrower in the case of 15 mm than in the case of 7 mm length core. The

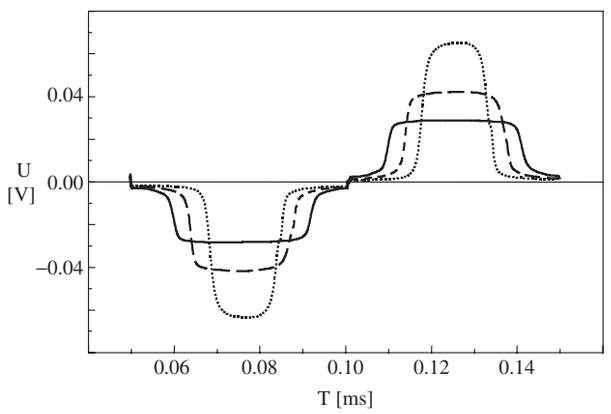

Figure 6. The induced voltages pulses in the pick-up coil in the case of 7 mm (solid line), 10 mm (dashed line) and 15 mm (dotted line) length core material at 10 kHz frequency driving field. Reprinted with permission from [127], G. Vértesy and A. Gasparics, *J. Electrical Engineering* 53, 53 (2002). © 2002, Slovak University of Technology.

Table 2. The necessary amplitude of driving field and the relative sensitivity (S). Reprinted with permission from [127], G. Vértesy and A. Gasparics, *J. Electrical Engineering* 53, 53 (2002). © 2002, Slovak University of Technology.

Core length	7 mm	10 mm	15 mm
Driving field [%]	100	72	52
S [%]	100	140	190

amplification of the sensor is larger when the amplitude of the driving field is lower, because the sensor compares the measured field to the driving field. The calculated relative sensitivities (S) can be seen in Table 2. If the driving field is decreased according to Fig. 6, the base of the calculation was the amplitude of the driving field in case of 7 mm length core.

The amplification depends not only on the amplitude of the driving magnetic field. In the case of the same driving field the sensitivities were measured by a dc magnetic field, which was generated by the driving coil with dc component driving current in it. During this measurement the time-shift was recorded. This time-shift with respect to the time of the magnetization cycle can be seen in Fig. 7 as a function of the measured dc magnetic field in case of 7, 10 and 15 mm length core.

The measurements were performed by studying the signal of the pick-up coil. As it is shown, a significant decrease of the width of induced voltage pulses was found with increasing core length, leading to the improvement of the sensitivity, through the possible decrease of the driving field amplitude. The amplification of the sensor was also found (with fixed driving field amplitude) to increase if the length of the core is increased. In the case of 15 mm length core about 90% increase of sensitivity was observed, with respect to the case of 7 mm length core.

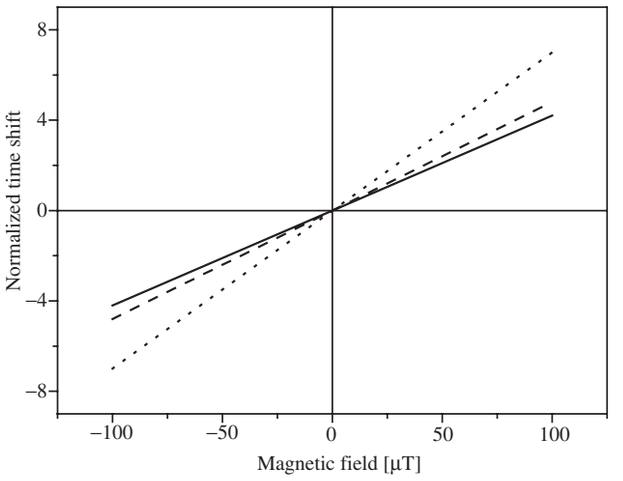

Figure 7. The amplification of the Fluxset sensor in the case of 7 mm (solid line), 10 mm (dashed line) and 15 mm (dotted line) length core material at 10 kHz frequency driving field. Reprinted with permission from [127], G. Vértesy and A. Gasparics, *J. Electrical Engineering* 53, 53 (2002). © 2002, Slovak University of Technology.

There are also some more variable parameters of the sensor (for example, pick-up coil length, driving coil length, solenoids diameter) and some relationships between the parameters (for example the ratio of the driving coil length and the core length), which could be useful in the future for testing of the sensor model, however the influence of these parameters have not been investigated yet.

On the base of the experimental results, quantitative determination of the sensitivity of a given arrangement can be done. Increasing the core length up to 40 mm, 10 pT resolution can be achieved. In majority of eddy current testing applications short, 5 mm core length is advantageous, however even in this case 10–20 nT sensitivity can be achieved, which is fairly enough for good sensitivity detection of material inhomogeneities.

3.5. Characterization of Fluxset Sensor

Based on the above considerations, it turned out clearly, that different types of sensor should be developed for high sensitivity and for high frequency applications. The demand of the application determines, which version can be applied most successfully.

3.5.1. High Sensitivity Version of the Sensor

The high sensitivity version operates in dc or in low frequency ac (below 100 Hz) range, the size of the probe is relatively large (20–40 mm). The output signal of the sensor as a function of magnetic field is shown in Fig. 8. The linearity is better than 1%, the calibration is 0.12 mV/1 nT. Reference measurements were performed in the Tihany Geophysical Observatory, simultaneously using this version of the sensor and a standard observatory "Kvarc 2" type, torsion magnetometer. The change of the vertical component of the magnetic field of the Earth was measured through 24 h. The results are shown in Fig. 9. The low field stability and the large sensitivity of the device were proved by this measurement.

The low frequency and high sensitivity version of the sensor was tested by the detection of the generated magnetic field in natural (unshielded) environment. The sensor can produce one data in each period of the driving signal, so we can determine its bandwidth by the half of the driving frequency—which is 2.5 kHz in case of the applied

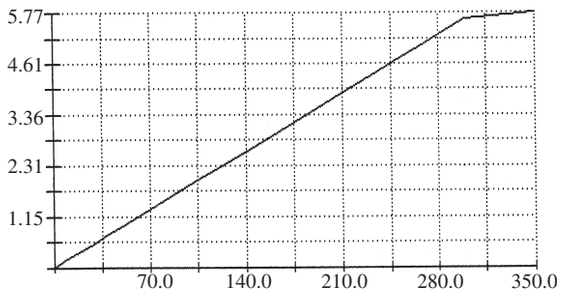

Figure 8. The calibration of Fluxset sensor. (Y axis: the output of the sensor in Volts, X axis: current of the calibration coil in mAmps, 1 mA = 156 nT). Reprinted with permission from [97], G. Vértesy, et al., *Sensors and Actuators A*, 85, 202 (2000). © 2000, Elsevier.

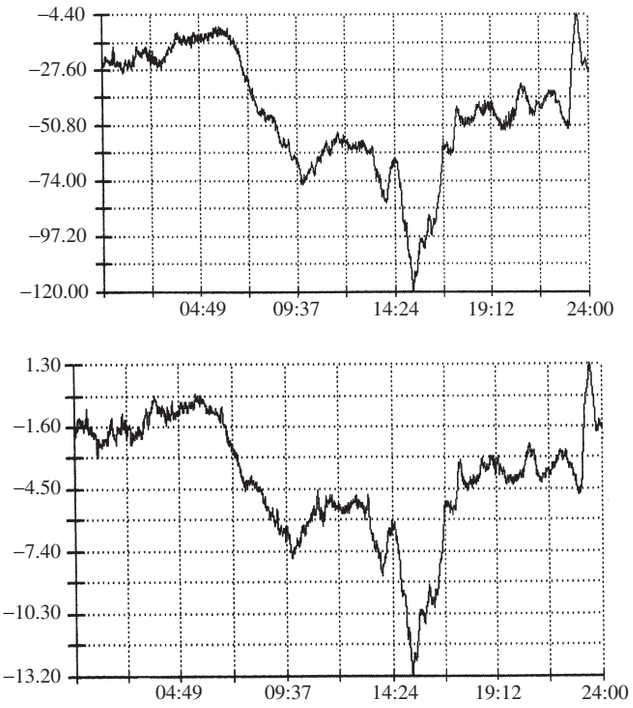

Figure 9. The change of the Earth's magnetic field, simultaneously measured by a standard observatory magnetometer (above), and by the Fluxset sensor (below). The outputs of both magnetometers are given in arbitrary units (Y axis), the time is given in hours (X axis). Reprinted with permission from [97], G. Vértesy, et al., *Sensors and Actuators A*, 85, 202 (2000). © 2000, Elsevier.

5 kHz frequency driving signal. The bandwidth of the whole measurement system (not only the probe) was reduced by increasing the applied time-constant of the lock-in amplifier. Three different arrangements were investigated in order to determine the noise limited sensitivity of the sensor. The noise signal of the whole measurement system (*System noise*) was recorded when the sensor had no core material. After that, the core was inserted into the sensor and the noise of the external magnetic field together with the system noise was detected (*Measured noise*). Additional sinusoidal magnetic field with 1 nT amplitude at 2 Hz was applied in order to calibrate the output signal of the measurement system (*Measured field*). The results of these measurements can be seen in Fig. 10. It can be well observed that in this case the noise became much larger. The source of this noise can be the noisy magnetic environment, or it can origin from the ferromagnetic core by itself. The sensitivity of the sensor was determined by the spectral analysis of the detected signals. The system has approximately 20 Hz bandwidth so this frequency range was investigated. The amplitude spectrums can be seen in Fig. 11. The calculated average levels of the noise and its 2 Hz frequency component together with the equivalent magnetic field value are summarized in Table 3.

The results show that the noise limited sensitivity of the measuring system, which means, how small signal can be separated from the noise, is in the range of 10–50 pT. (The measured magnetic noise of the environment is two

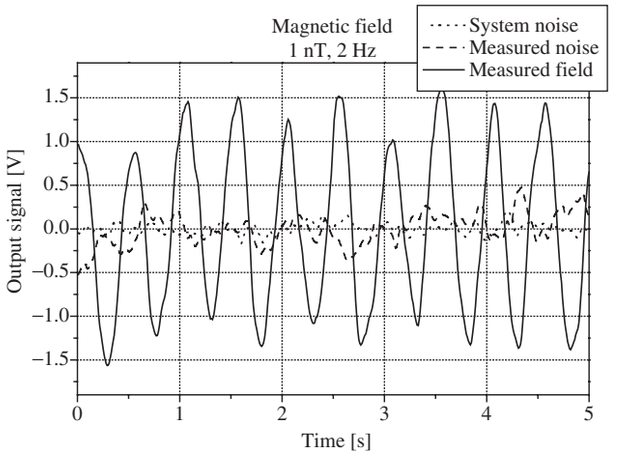

Figure 10. The amplitude spectrum of the detected signals. Reprinted with permission from [97], G. Vértesy, et al., *Sensors and Actuators A* 85, 202 (2000). © 2000, Elsevier.

or three times higher: 50–150 pT.) The reachable level of the sensitivity depends on the bandwidth of the measurement system obviously: the smaller the bandwidth, the larger the reachable sensitivity is, e.g., in Fig. 11, where the bandwidth was 20 Hz, 56 pT resolution was detected. By decreasing the bandwidth down to 1–2 Hz, 10 pT resolution can be achieved (7.6 pT at 2 Hz; see Table 3.) In general, it can be concluded that Fluxset sensor has about 100 pT sensitivity, which can be higher or lower in accordance with its application.

The temperature dependence of the output signal of the probe (the measuring head only) was measured, keeping the probe in fixed position in the laboratory, without magnetic shielding. The temperature of the probe was modified from −196 °C till 200 °C, and the output signal was measured by 5 s sampling. The time of the complete measurement was 70 min. The result of the measurement is shown in Fig. 12. In this case the sensor was in large external magnetic field

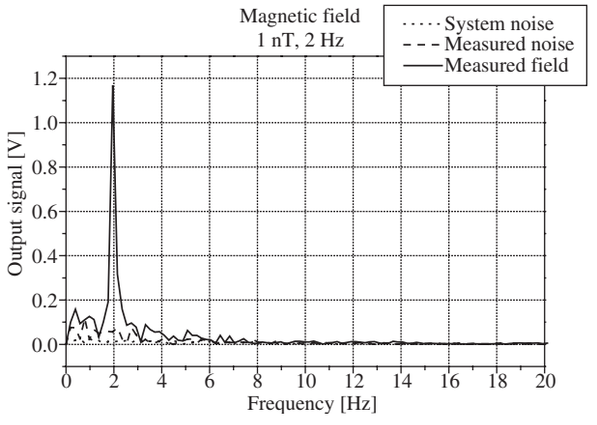

Figure 11. The time dependent output signal of Fluxset sensor. Without core (System noise), with core (Measured noise) and in the presence of 1 nT amplitude ac magnetic field (Measured field). Reprinted with permission from [97], G. Vértesy, et al., *Sensors and Actuators A* 85, 202 (2000). © 2000, Elsevier.

Table 3. The calculated average levels of the noise and its 2 Hz frequency component together with the equivalent magnetic field values. Reprinted with permission from [97], G. Vértesy, et al., *Sensors and Actuators A*, 85, 202 (2000). © 2000, Elsevier.

Measured signal:	Determined [V]	Calibrated [pT]	Determined at 2 Hz [V]	Calibrated at 2 Hz [pT]
System noise	0.06554	56.1	0.0089	7.592
Measured noise	0.18094	154.9	0.0564	48.300
Measured field	1.16832	1000	1.1683	1000

during the measurement, and Fig. 12 shows that the output signal in this resolution doesn't depend on the temperature of the probe. However, this measurement shows only the large field temperature stability of the probe. To get information about the temperature dependence of the noise, the noise was also measured, similarly to the measurement shown in Fig. 11, as a function of the temperature, at three temperature values (−196 °C, −97 °C and +20 °C), and the amplitude spectrums were calculated. The result is shown in Fig. 13. In this case 0.8 Hz frequency pulses were used instead of the sinusoidal excitation. The temperature dependent measurements proved the large thermal stability of the probe considering both the average level of the output signal and the noise of the device.

3.5.2. High Frequency Version of the Sensor

In certain application areas, a wide frequency range of operation is needed, and the extremely high sensitivity is not so important. A high frequency version was developed mainly for the application in eddy current testing (see below). By decreasing the size of the sensor core the frequency range of the sensor was extended up to 200 kHz driving frequency, which makes possible to measure ac magnetic fields of up to 100 kHz frequency. In this version the size of the probe is small (5 mm), and the sensitivity is not so high as in the case of the other version (10 nT). The other main advantage of this version is the high spatial resolution.

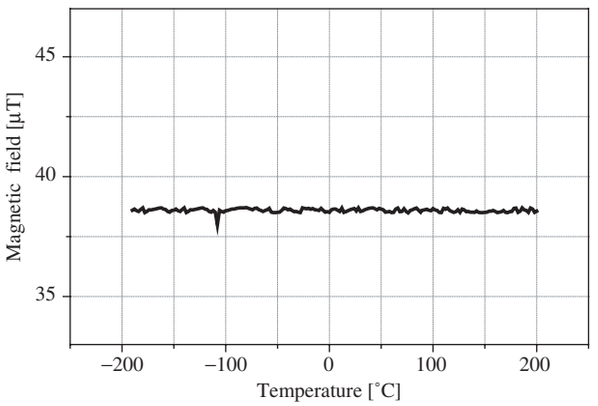

Figure 12. Temperature dependence of the output signal of the probe. Reprinted with permission from [97], G. Vértesy, et al., *Sensors and Actuators A* 85, 202 (2000). © 2000, Elsevier.

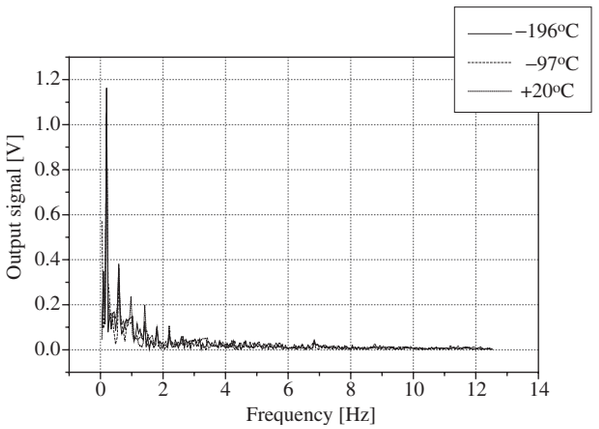

Figure 13. The temperature dependence of the amplitude spectrum of the detected signal. Reprinted with permission from [97], G. Vértesy, et al., *Sensors and Actuators A* 85, 202 (2000). © 2000, Elsevier.

4. APPLICATION OF FLUXSET SENSOR

Fluxset sensor can be used very well for geophysical, geological applications and in detecting of low and middle frequency electromagnetic smog. In differential mode of operation this device is suitable for the measurement of stray and residual fields, which makes possible to detect the presence of different ferromagnetic impurities in the non-ferromagnetic materials. By the application of a sensor matrix the magnetic image of different objects can be taken. Because of the negligible transverse sensitivity, 3D magnetometers can be built using Fluxset sensors. The advantageous properties of the high frequency version of the sensor (relatively large sensitivity, relatively wide frequency range, small size, and good spatial resolution, together with the simple construction) make this device ideal in eddy current testing [129].

4.1. Eddy Current Testing

Non-destructive measuring techniques, based on electromagnetic principle have become recently a common tool for investigation of material defects and degradation. The Fluxset sensor can be effectively utilized for the detection of defects in conducting materials using eddy current testing (ECT) measurements. Eddy current testing is one of the most frequently used nondestructive testing methods. The magnetic field generated by eddy currents induced by an exciting coil in the tested components is monitored and its perturbation is considered as an indication of an internal defect. In a conventional ECT system the field perturbation detector is the exciting coil itself. Most of the present-days magnetic field sensors used in ECT are inductive devices. The shape and size of the detected defect can be calculated from the measured signal [130–133]. The sensitivity of conventional inductive sensors is proportional to the field frequency, and therefore they cannot be used at low frequencies. This is why the commercial ECT systems are sensitive mainly for defects on the surface of the tested component, as high frequency electromagnetic field is being attenuated in depth.

In order to eliminate this disadvantage, but to save the simplicity and the low cost of ECT method, Fluxset sensor was used in ECT magnetic field measurements [134]. The principle of this technique is based on the combination of the detection of changes in the eddy current magnetic field and the variation of magnetic polarization of the sample due to the presence of the defect.

The ECT probe is constructed by attaching the Fluxset probe to an exciting coil. Depending on the thickness, electrical conductivity and relative magnetic permeability of the sample, the optimal exciting frequency is typically in the 1–100 kHz range. The main advantage of the presented technique compared to the conventional ECT methods is the significantly improved sensitivity and lateral resolution in the X and Y directions, simultaneously. Considering that the sensitivity of the device is not dependent on the frequency, the exciting frequency of the eddy current measurement can be reduced, obtaining such a way information from the deeper region of the sample to be investigated. By scanning the ECT probe over the sample surface the magnetic image of the sample can also be obtained. Figure 14 illustrates the scheme of the eddy current measurement system.

4.1.1. Quantitative Eddy Current Testing Using Field Probe

A numerical tool was developed, which was able to fully simulate an ECT apparatus based on a Fluxset sensor [135]. The resulting tool is extremely useful in understanding more

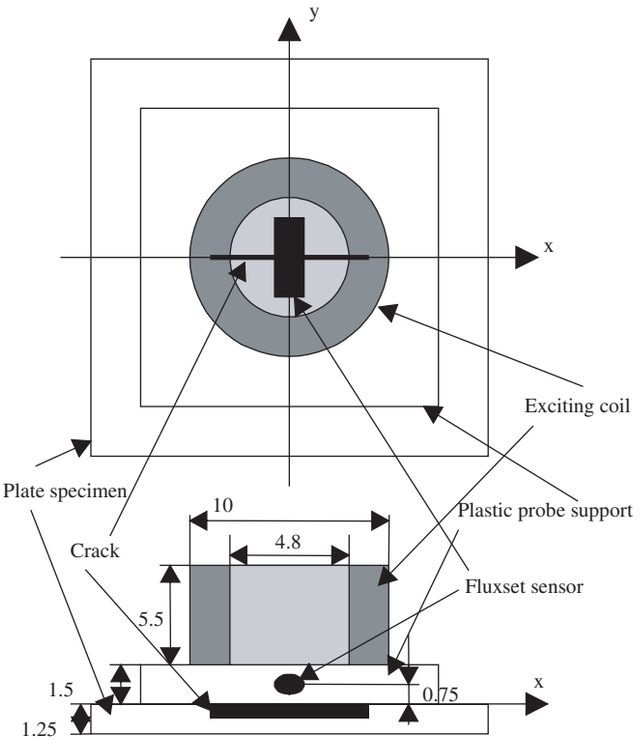

Figure 14. Fluxset type eddy current probe over a square shape plate specimen containing an ID type crack. Top and cross-sectional views. Reprinted with permission from [139], J. Pávó, et al., *Sensors and Actuators A* 110, 105 (2004). © 2004, Elsevier.

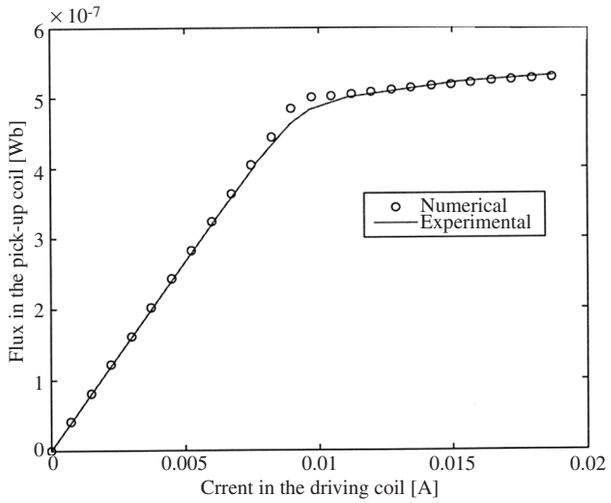

Figure 15. Numerical and experimental flux-current curve for the Fluxset sensor (after [135]). Reprinted with permission from [135], R. Albanese, et al., in "Electromagnetic Nondestructive Evaluation (IV)" (S. S. Udpa, T. Takagi, J. Pavo, and R. Albanese, Eds.), p. 58. IOS Press, Amsterdam, 2000. © 2000, IOS Press.

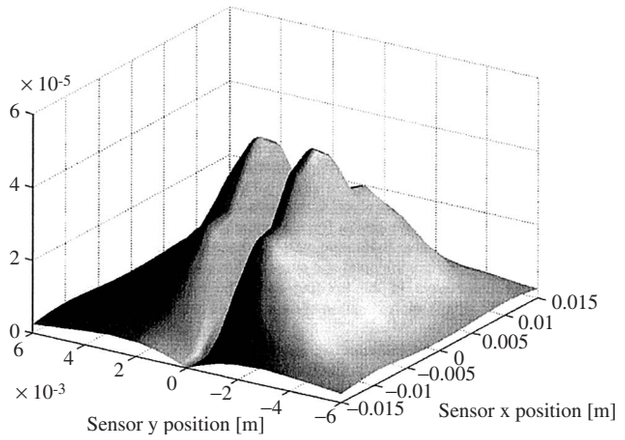

Figure 16. Amplitude of the magnetic field perturbation due to a crack located in the $y = 0$ plane, from $x = -4.5$ mm to $x = +4.5$ mm. Reprinted with permission from [135], R. Albanese, et al., in "Electromagnetic Nondestructive Evaluation (IV)" (S. S. Udpa, T. Takagi, J. Pavo, and R. Albanese, Eds.), p. 58. IOS Press, Amsterdam, 2000. © 2000, IOS Press.

deeply the behavior of the sensor in a typical ECT application (i.e., in the presence of the exciting coil and the cracked specimen). This is fundamental if the inverse problem (given the measurements provided by the sensor, find the crack) must be solved. A non-linear model of the sensor was coupled to a numerical scheme able to simulate the effects of cracks in conducting bodies in terms of magnetic field perturbation. For the non-linear model of the Fluxset sensor a finite element mesh (40 elements) of the core was given, and a piecewise linear B–H curve was assumed with only one breakpoint. In Fig. 15 the comparison is shown between the experimental and numerical traces of the flux in the pick-up coil as a function of the current in the exciting coil. The agreement is very good, especially considering the simple approximation of the magnetic characteristics used.

The perturbation of the magnetic field, due to a thin rectangular crack (length 9 mm, depth 0.75 mm) was simulated in a 1.25 mm thick INCONEL 600 specimen. (The border effects were taken negligible.) A pancake-type coil (inner diameter 8.5 mm, outer diameter 3.5 mm, height 5 mm, lift-off 0.5 mm, 110 turns fed with 120 mA rms at 20 kHz) was used to induce the eddy currents in the body. The magnetic field sensor is placed in the y direction (normal to the crack plane) 0.5 mm above the specimen, centred on the exciting coil axis. Thanks to superposition, only the region close to the crack must be meshed. The meshed volume was 30 mm × 8 mm × 1.25 mm; the mesh was made of 1200 hexahedral elements, with 1266 degrees of freedom. The unperturbed solution was computed analytically. In Fig. 16 the amplitude of the magnetic field perturbation is shown, as a function of the two spatial co-ordinates x and y. The crack is located in the $y = 0$ plane, from $x = -4.5$ mm to $x = +4.5$ mm. One key feature, which is worth of noticing is, that the magnetic field perturbation in the y direction vanishes, for symmetry reasons, at the crack plane, while the other components (as well as the impedance variation signal) usually have a maximum. This property can be very useful when detecting the crack plane prior to the proper crack shape identification [136].

4.1.2. Design of Fluxset Probes Addressed to the Detection of Deep Defects

Recently a set of tools has been presented for the optimization of the Fluxset probe for eddy current testing addressed to the detection of deep defects [137]. These tools allow prediction and comparison of the performance of different Fluxset probes, i.e., a quick but reliable estimation is given of the signal-to-noise ratio as a function of frequency, expected tilting error, defect extent and depth. The objective function to be described is envisaged to be related to the signal-to-noise ratio. The investigated probe consists of an exciting coil and a Fluxset field sensor, placed at the center of the exciting coil, parallel to the plane of the specimen to be tested, as shown in Fig. 14. In the absence of defects and far from the edge of the specimen, the output signal should in principle be zero. This feature should improve the capability to detect "deep" defects, i.e., beyond the depth of penetration of the standard ECT inductive coils.

a. Signal Due to a Small Spherical Defect Embedded in a Metallic Plate The unperturbed eddy current distribution induced in an infinite plate with finite thickness can be computed either numerically or analytically [138]. Once the eddy current density is known at the defect location, the effect of the flaw can be simulated by superimposing a small current flowing in the opposite direction. The eddy current and magnetic field distributions in the presence of a defect can be obtained via superposition using the dyadic Green functions. At a distance from the defect, the field perturbation generally approaches the dyadic Green function multiplied by a suitable factor k.

In the case of a small spherical defect (e.g., due to a gas bubble trapped in the metal during a welding process), at

low frequencies, this factor is shown to be:

$$k = 3J_0V_d \tag{11}$$

where J_0 is the unperturbed current density at the defect location, and V_d is the volume of the spherical defect.

b. Effects of Defect Shape, Location and Extent As far as the shape is concerned, experimental data as well as 3D numerical analysis show that a cylindrical defect having radius r and height h is roughly equivalent to a sphere having the same volume, provided that $r \leq h \leq 2r$. As indicated in (11), for small spheres the signal scales with the volume, rather that its cross section. The influence of the vertical location of the defect on the signal has been studied at various frequencies. The results can be seen in Fig. 17 refer to the Fluxset probe shown in Fig. 14 placed above a 50 mm thick stainless plate with a spherical defect having a radius of 1.5 mm located at 14 mm from the coil axis.

c. Effects of Tilting and Positioning Error of Sensor and Probe The major source of noise is assumed to be related to the tilting of the probe. This effect can be estimated either analytically or numerically. The analytical estimates are trivial at zero and infinite frequency. Analytical estimates are also possible at finite frequencies using the dyadic Green functions, but the calculation is rather awkward, as the integration has to be carried out over the region covered by the coil turns.

The numerical calculation is cumbersome as well, as the tilting makes the problem three-dimensional. An approximate estimate of the tilting effect at various frequency can also be obtained by analyzing a 2D planar problem, which has the advantage to remain 2D even in the presence of a tilting. The effect of the 2D approximation can then be quantified by comparing the 2D results with 3D analytical calculations in particular cases. The results and the experimental data collected when scanning plates with and without defects, allows to estimate that the variation of the tilting angle during a scan is in the order of 0.01°.

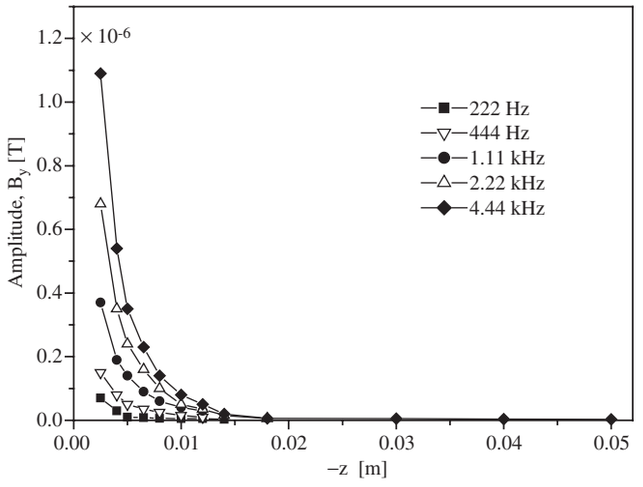

Figure 17. Influence of frequency and vertical location of the defect. Perturbation of the horizontal magnetic field on the axis of the inducing coil at $z = 0.62$ mm due to a spherical defect having a radius of 1.5 mm located in a 50 mm thick stainless steel plate at 14 mm from the coil axis (after [137]). Reprinted with permission from [137], R. Albanese, et al., in "Electromagnetic Nondestructive Evaluation (VIII)" (T. Sollier, D. Premel, and D. Lesselier, Eds.), p. 52. IOS Press, Amsterdam, 2004. © 2004, IOS Press.

Horizontal displacement simply introduces offset. Vertical displacements increase lift-off and slightly reduce the signal. For instance, there is a 5% signal reduction for a 0.2 mm (30%) increase in the lift-off of the sensor for a 13.5 mm deep defect in a 50 mm stainless steel plate at 2.22 kHz. x- and y-displacements simply introduce offsets. Coil tilting T_x modifies the induced eddy currents: $\Delta J_0/J_0 \approx \mathrm{O}[\sin(T_x)]$. Sensor tilting T_x modifies the signal: $\Delta B_{y\,\mathrm{def}}/B_{y\,\mathrm{def}} \approx \mathrm{O}[\sin(T_x)B_{z\,\mathrm{def}}/B_{y\,\mathrm{def}}]$. For a 13.5 mm deep defect $\max|B_{z\,\mathrm{def}}|/\max|B_{y\,\mathrm{def}}| \approx 2$ for a wide range of frequencies.

d. Optimization of the Fluxset Probe Methods and results described in [137] show that it is possible to estimate the signal-to-noise ratio (S/N) at a given frequency as a function of the vertical position of the defect. It is then possible to optimize the parameters of a given coil and propose alternative probe designs, like the compensation coil probe. For instance, where the inducing field is provided by two concentric solenoids yielding a low horizontal and vertical field in the region around the axis where the sensor has to be located.

The expected magnetic field distribution and signal can be determined analytically, numerically and/or experimentally for the investigated specimens/defects with and without the presence of the displacement/tilting error: $s(\Delta x, \Delta y, \Delta z, T_x, T_y, T_z)$. The error suppression objective function S/N can for instance be defined as the reciprocal of the first order signal energy derivative, e.g., for a Δx displacement:

$$S/N_{\Delta x} = \frac{1}{\frac{\sqrt{E[s(\Delta x,0,0,0,0,0)]-E[s(0,0,0,0,0,0)]}}{\sqrt{E[s(0,0,0,0,0,0)]}\cdot\Delta x}} \tag{12}$$

4.1.3. Calibration of the Sensor in Spatially Strongly Inhomogeneous Magnetic Fields

Spatial resolution is a very important quality factor of sensors used for the measurement of spatially inhomogeneous magnetic fields, as is the case in eddy current testing. It is obvious that a sensor having finite dimensions cannot measure the magnetic field only in one single geometrical point and—as the magnetic field is not the same along the sensor—it is important to know what is the output of the sensor if it is applied for the measurement of different inhomogeneous magnetic field patterns. Because of this, a procedure was developed for the calibration of Fluxset sensor in spatially strongly inhomogeneous magnetic field [139, 140]. The goal of this procedure is to give a rule to predict the sensor output if a given inhomogeneous field is measured. The inhomogeneous magnetic field used for the calibration was produced by eddy currents around an artificial crack, located in a flat plate, made of conductive material. This calibration is important for the application of this magnetic field sensor in the nondestructive material evaluation, using the eddy current method, because the output signal of the

magnetic probe can be used quantitatively only if the output of the actual probe is related to the measured magnetic field distribution. This is the basic requirement for the application of any optimization method targeting the reconstruction of the defect detected by measurements.

The relation between the output of the Fluxset sensor and the spatial distribution of the measured magnetic field was established through the numerical and experimental investigation of the interaction of a Fluxset type ECT probe and a crack in a finite plate specimen. For this reason, the measured signal of the sensor was compared with the calculated magnetic field when the actual measuring set-up was rigorously modeled. The interaction of the probe and the given crack in the finite plate was calculated using numerical field calculation methods (Finite Element Method and Boundary Integral Method) by superimposing the results obtained for a finite plate without cracks and a crack in an infinite plate [131, 132, 141, 142].

The relation between the experimentally measured output and the calculated magnetic field distribution was obtained by the evaluation of several calibration factors giving the best fit of the calculated and measured data. As a result, a numerical procedure was established that could predict the output of the sensor if an arbitrary magnetic field distribution was given [139]. The important novelty of the developed method is that the calibration of the studied magnetic sensor is given in the case of a spatially strongly inhomogeneous magnetic field. Although the procedure is demonstrated with the calibration of Fluxset type ECT probe, the same method can be used for other type of magnetometers, too.

The studied eddy current nondestructive testing arrangement is shown in Fig. 14. The cylindrical exciting coil carries a 20 kHz sinusoidal current and its position scans along $y =$ constant lines parallel to the plate. The Fluxset sensor, which is attached to the exciting coil, measures that component of the magnetic field that is parallel to its axis. The size of the rectangular plate specimen is 80 mm $\times$ 80 mm, the other dimensions of the arrangement are given in Fig. 14 in mm units. There is a crack in the x-direction in the middle of the plate. The crack is actually a 9 mm long 0.2 mm thick 0.25 mm deep artificial notch made by electric discharge machining (EDM notch). The crack might be either on the same (so-called ID crack) or on the opposite (so-called OD crack) sides of the plate with respect to the probe.

The core material is periodically magnetized to saturation in both directions by the triangular current excitation, $i_d(t)$, of the driving coil (Fig. 3). Considering the idealized magnetization curve of the core material shown in Fig. 2, we can see that the induced voltage impulse in the pick-up solenoid, $v_s(t)$, is almost zero when the core is saturated, on the other hand this induced voltage has a relatively large value (proportional to the time derivative of the driving current) while the driving magnetic field changes its direction (i.e., the core material is magnetized in the linear range). If an external magnetic field (i.e., the field to be measured) is superimposed on the periodic driving magnetic field, the time spent in saturation in one direction is longer than the time spent in saturation in the other direction, consequently the impulse, $v_s(t)$, is shifted. The time shift of the impulse, $v_s(t)$, can be accurately measured, as a result the external field can be predicted. One can see that the measured magnetic field is actually the field of the sensor core. Since the volume of the sensor core is very small, we assume that it does not significantly disturb the magnetic field to be measured, consequently the sensor measures approximately the magnetic field that can be detected around its core if we neglect the disturbing effect of the presence of the sensor core.

The output signal is approximated as the weighted sum of the field values calculated theoretically around the sensor. The weighting coefficients are obtained by finding the best fit of the actual experimental output and the theoretical prediction of the measured field in the least square sense. As an example, the real and the imaginary parts (that is the values of the time function being shifted in phase with 0° and 90° with respect to the exciting current of the pancake coil, respectively) of the y component of the crack field of a 9 mm long, 0.25 mm deep ID crack are shown in Fig. 18. For easier understanding, in these figures the locations of the crack and a 10 mm long Fluxset sensor are also shown.

As we see from Fig. 18, the magnetic field perturbation around a crack excited by a small pancake type induction coil is spatially strongly inhomogeneous. The typical length of a Fluxset sensor used for the measurement of this field perturbation is between 5 and 15 mm, so the magnetic field along the sensor takes various different values. Consequently, we cannot tell from the output what is the actually measured field data are. Note that the calibration curves given by sensor manufacturers are usually taken in spatially homogeneous fields, so these curves do not provide sufficient information for the quantitative utilization of the output signal in the case of special applications like, for example, our eddy current testing application. This is the

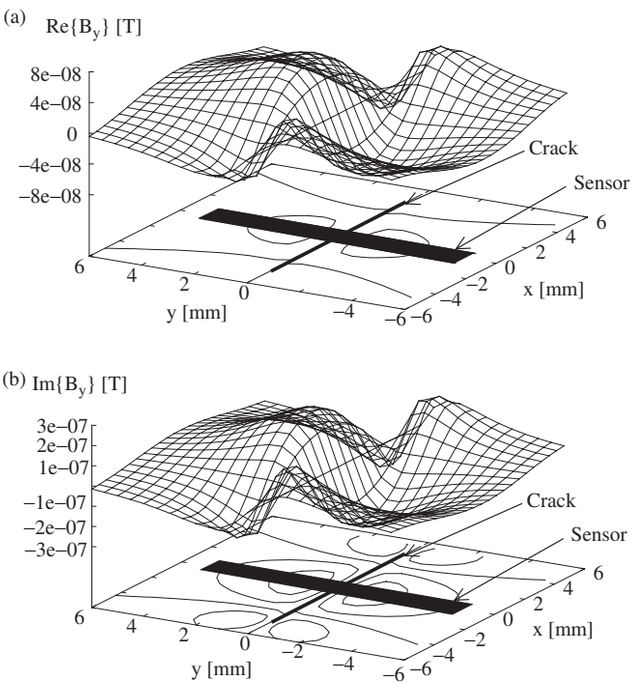

Figure 18. y component of the magnetic flux density around the sensor when the probe is at the $x = 0$, $y = 0$ position. (a) real part, (b) imaginary part. Reprinted with permission from [139], J. Pávó, et al., *Sensors and Actuators A* 110, 105 (2004). © 2004, Elsevier.

reason why we are trying to introduce a better and more complete way for the prediction of the output signal that can be applied also for the quantitative measurement of inhomogeneous magnetic fields.

In our model we assume that the output of the sensor is linearly proportional to the magnetic field values calculated along the sensor when the disturbing effect of the presence of the sensor is neglected. The output of the Fluxset sensor is predicted to be the weighted sum of the calculated field values around the sensor. The weighting coefficients are calculated by finding the best fit to the actual experimental output signal in the least square sense. Assume that the magnetic field is calculated in M locations along the Fluxset sensor and N different sensor positions around the crack are considered to get the weighting coefficients (N is typically larger than M). In other words we want to solve the equation,

$$\mathbf{Aw} = \mathbf{b} \tag{13}$$

where **b** is a column vector with N elements containing the measured output in the different sensor positions and **w** is a column vector with M elements containing the unknown weighting coefficients associated with the various measured field values along the sensor. **A** is a matrix with N rows and M columns, each row of **A** contains the calculated magnetic field values along the sensor in the given sensor position. Since $M < N$, the given equation system can be solved in the least square sense after left multiplying it with the transpose conjugate of **A**.

The calibration procedure can be demonstrated by examples. First we assume the measurement that results are shown in Fig. 19. In this figure the real and imaginary parts of the sensor output are shown while the probe is scanning above specimen. The position of the probe is represented by the co-ordinates of the axis of the exciting coil that is with the location of the central position of the probe. In Fig. 19 the sensor output versus the location of the sensor is shown.

As a first rough calibration we assume that the output of the sensor is determined by only one magnetic field value, namely the y component of the sum of the edge and crack fields at the middle of the sensor. This assumption means that in (13) **w** is a scalar, that is $M = 1$. In Fig. 20 the real and imaginary parts of the predicted sensor output are shown. The RMS error, E, of the prediction is 45.6% that is calculated as,

$$E = \sqrt{\frac{\sum_{i=1}^{K} |S_m - S_p|^2}{\sum_{i=1}^{K} |S_m|^2}}, \tag{14}$$

where S_m and S_p denotes the measured and predicted sensor output, respectively. K is the number of measurement points in the whole scan. Although the obtained prediction error is quite large, we can see by comparing Figs. 19 and 20 that the given prediction can be accepted as an agreeable qualitative result. In fact this result is very close to the one that can obtain by multiplying the magnetic field in the middle of the sensor with the calibration factor measured in homogeneous field.

A better calibration result was obtained when the weighted sum of the field values measured in five points

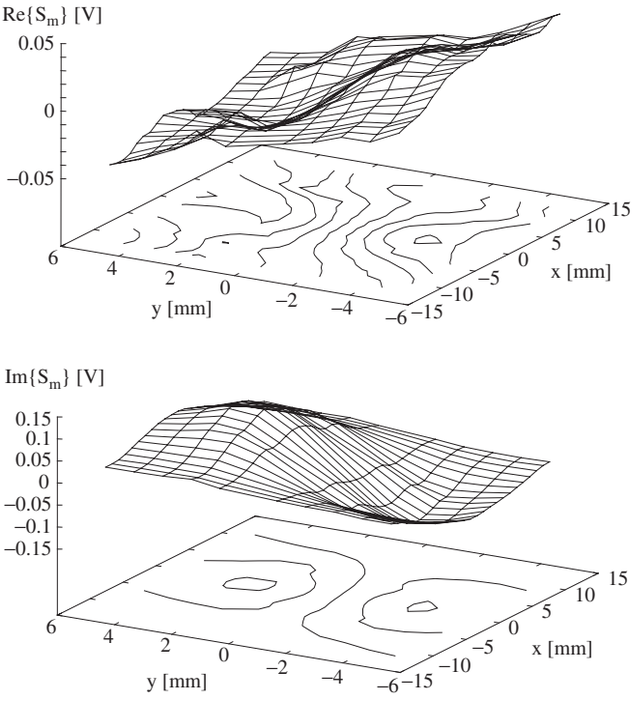

Figure 19. Measured sensor output. (a) real part, (b) imaginary part. Reprinted with permission from [139], J. Pávó, et al., *Sensors and Actuators A* 110, 105 (2004). © 2004, Elsevier.

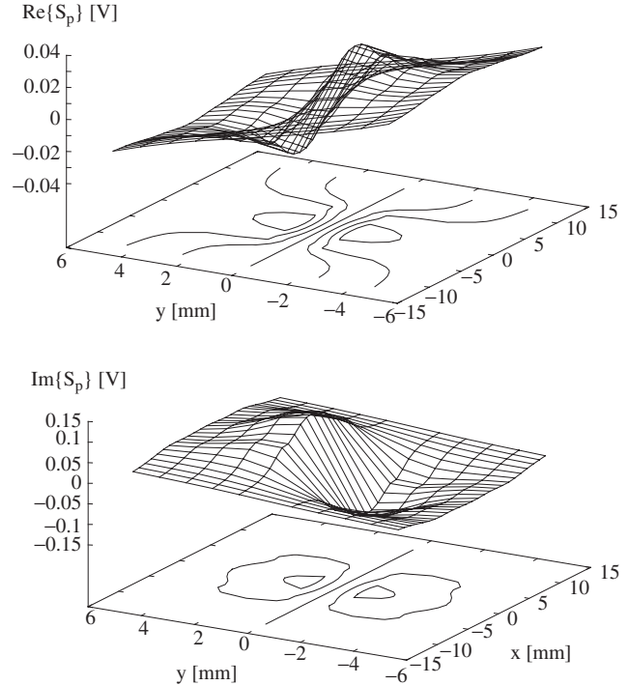

Figure 20. Sensor output prediction based on one field point. (a) real part, (b) imaginary part. Reprinted with permission from [139], J. Pávó, et al., *Sensors and Actuators A* 110, 105 (2004). © 2004, Elsevier.

along the sensor are used to form the sensor output prediction [139]. Of course, based on the presented example, this statement is proved only for the kind of spatial distributions that are related to material defects, so this can be used mostly for ECT measurements, however we believe that the basic idea and the way of calibration can be used for rather wide class of real technical problem. The only thing that we have to keep in mind is that the calibration should be done by the rigorous numerical and experimental study of the problem for the actually calibrated sensor is intended to be used.

4.1.4. Separation of Signals and Noise Filtering Using Neural Networks and Signal Processing

Signal processing can be used to extract significant indications from the set of raw measurements representing the output of the probing system. The following operations were successfully done by signal processing:

- Gaussian noise suppression/reduction: multiresolution image processing was used to reduce the effects of noise on the measurements; the 2D wavelet analysis has showed itself a powerful tool to perform a time-frequency filtering of the input data. The method was applied for Fluxset data [143].
- Edge-effect reduction/suppression and image enhancement: a system based on neural network was applied to remove the edge effect from the measured data. When the input signal is processed without an enhancement technique, the performance of the defect reconstruction system is very poor. Since the power content of the defect signal is very low with respect to the power content of the edge-effect signal, the defect reconstruction system is usually not able to extract the crack from the background of the measurement. The edge effect was removed by using a system based on the extraction of independent components from the input data, without any *a priori* knowledge on the input data [144].

4.1.5. Comparison of Various Probes, Evaluation of the Benchmark Measurements

An extensive experimental campaign was done to evaluate the performance of Fluxset probes compared to other probes available on the market and in research laboratories [145, 146]. Several benchmark measurements were carried out with various probes. Measurements were performed by three different measuring heads and the results were compared with each other. These were the Fluxset ECT head, a conventional, but increased sensitivity double ring ECT probe [147], and a standard JSAEM inductive probe. In order to reduce the ambiguity due to possible specimen imperfections, the evaluations were carried out on the same samples, e.g., an INCONEL 600 plate with one artificial crack and an aluminum plate with three slots (certified by the Italian Standard Organisation according to the standard UNI 9190/2-2). The conclusion of the measurements can be summarized as follows:

- The JSAEM probe was unable to detect OD slots in the UNI sample at all, the double ring probe was able to detect only the 30% slot in the UNI sample while Fluxset detected the 12.5% slot. The JSAEM probe was unable to detect OD20% crack in the INCONEL 600 specimen, while the Fluxset probe and double ring probe can easily detect even OD10% crack as well.
- The Fluxset probe has a signal about two orders of magnitude larger than that of the double ring probe, and its spatial resolution is also better.
- The Fluxset probe has similar S/N factor in general to the JSAEM coil probe in the case of the INCONEL 600 specimen, but the S/N ratio of Fluxset probe in the case of the smallest crack was significantly better.
- The JSAEM probe gives better scan results in case of ID type crack detection on UNI sample from point of view of the signal/noise ratio, due to the higher frequency of eddy current excitation in the case of JSAEM coil.
- The performance of the Fluxset probe (in terms of signal to noise ratio, spatial resolution and depth sensitivity) was found to be comparable and often better (especially in depth sensitivity) than the existing alternative probes, mainly thanks to the good behavior of the Fluxset sensor at low frequencies.

4.1.6. Examples of Eddy Current Measurements

a. Detection of Cracks in Stainless Steel Plate Measurements were performed using this technique on nonferromagnetic 1.27 mm and 5 mm thick, INCONEL 600 stainless steel plates [148, 149]. Artificial, rectangular shape EDM made cracks had been made previously on one side of the samples. The used sample, having a 10% deep crack (compared the depth of the crack with the thickness of the specimen) is shown in Fig. 21. The measurements revealed that 10% deep cracks on one side of the specimen could be identified easily from the reverse side (OD 10% crack). Cracks having different dimensions produce different image contrasts after data acquisition, which makes possible to reconstruct the size and the position of the crack by evaluating a series of images taken at different frequencies.

The surface distribution of the output signal of the ECT probe is shown in Fig. 22. Here the image of the crack is

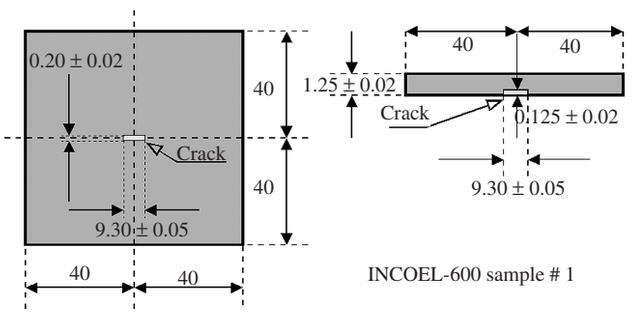

Figure 21. The specimen with a 10% artificial crack. The dimensions are given in mm. Reprinted with permission from [97], G. Vértesy, et al., *Sensors and Actuators A* 85, 202 (2000). © 2000, Elsevier.

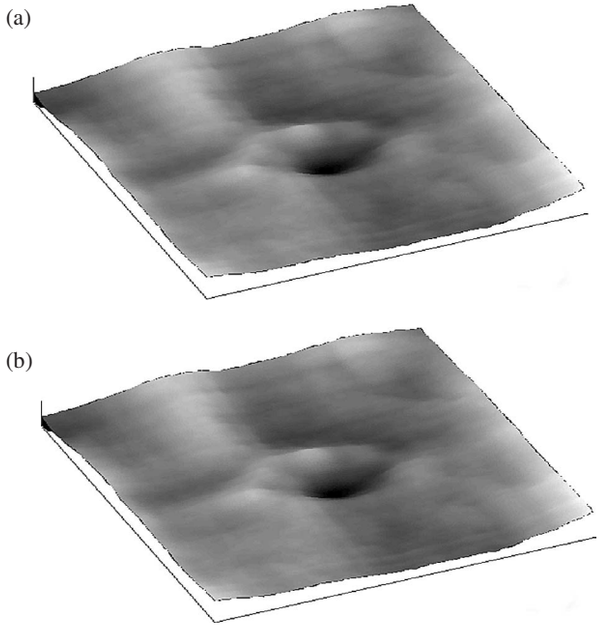

Figure 22. Images of a 0.125 mm deep artificial crack, detected from the back side, in the 1.25 mm thick INCONEL 600 sample, shown in Fig. 15. The measuring head was scanned over the surface of the sample. Sensor orientation is parallel (a) and perpendicular (b) with the length of the crack.

seen, obtained by scanning of the measuring head over the surface of the sample. The pictures were taken by two different detector orientations, with respect to the crack direction. Sensor orientation is parallel (a) and perpendicular (b) with the length of the crack.

A set of experimental ECT data, obtained by Fluxset type probe measuring INCONEL plate with rectangular thin crack, is analyzed in [150]. The working hypothesis was that the measured signals were linear mixtures of different sources: The signal related to the defect and the one related to the lift-off noise. This suggests that, on the basis of ICA technique (neural independent component analysis), a way can be envisaged to extract the defect signal. More formally, it was hypothesized that there existed two latent signals whose linear superposition with proper (unknown) weights give rise to the observed signals. In the model such latent variables are statistically independent, thus they might be separated through an ICA technique. Both separation performance and computational-complexity evaluations and comparison revealed that the proposed theory provided a good trade-off between performances and computational burden.

b. Detection of Air Bubble in Aluminum Plate To illustrate the capability of the technique for detecting not only small depth, but also small size defects (bubbles), three 1 mm thick aluminum plates were taken [151]. In one of them different size holes were fabricated. The specimen is shown in Fig. 23(a)]. Applying 970 Hz frequency excitation, the holes were detected from the top surface of the plates [see Fig. 23(a) and 23(b)]. Even the smallest, 0.35 mm diameter hole can be detected through the 2 mm thick aluminum

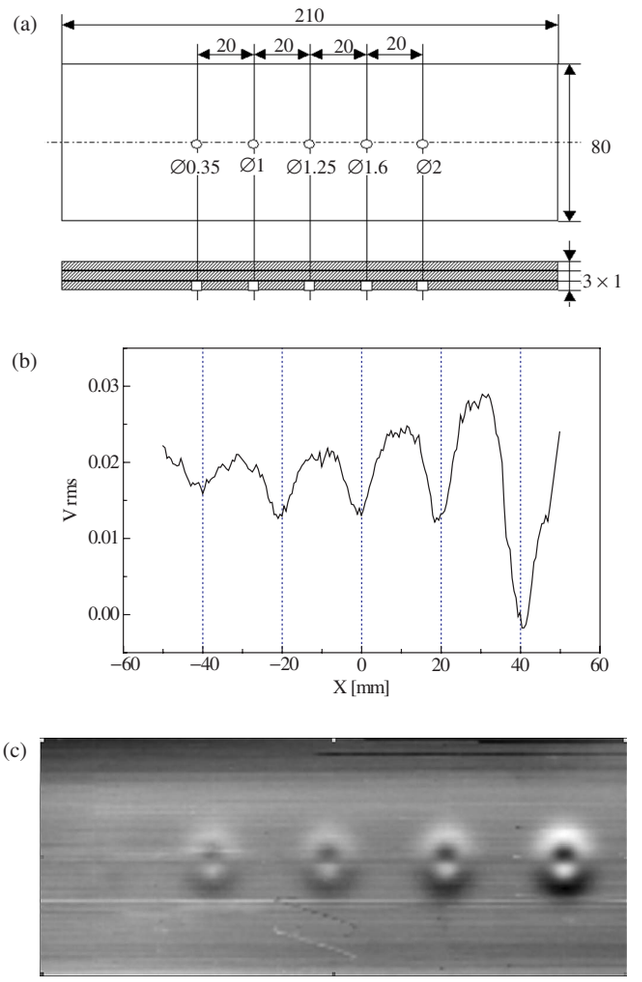

Figure 23. Specimen, which contains different size holes in a 1 mm thick aluminum plate, covered with two 1 mm thick aluminum plates. The dimensions are given in mm. (a). The output signal of the probe, measured on the upper side of the three-plates system along the line, 2 mm from the center of the specimen (b). The surface scan of the plate (c). Reprinted with permission from [151], G. Vértesy and A. Gasparics, *Mat. Sci. Forum* 414, 343 (2003). © 2003, Trans. Tech. Publications.

layer. The whole surface scan of the plate is shown in Fig. 23(c).

c. Detection of Cracks in Stainless Steel Tube Eddy current testing plays a crucial role in inspection of different tubes applied in power plants. One of the most important problems is the investigation of steam generator tubes in pressurized water-type nuclear power plants during their regulated periodic shutdown [152]. The limited frequency of the non-destructive inspections of the critical components during times of continuous operation makes it necessary to be able to follow the speed of the degradation or aging of the material from the very outset. Monitoring the changes in the material structure offers more reliable predictions about the macroscopic property of the inspected parts subjected to, for instance, mechanical stress or chemical corrosion. Therefore the real target of the non-destructive evaluation is the detection of small size flaws which are far

from the dimension which could be critical from a safety point of view.

The Fluxset based ECT probe was tested [153] on 5 mm long OD 10% and OD 20% circumferential and axial type artificial EDM cracks and on natural stress corrosion cracking (SCC) and intergranular attacking (IGA) type OD flaws in INCONEL 600 tubes (JSAEM Benchmark Specimens [154]). The reliability and the signal-noise performance of the experimental set-up were investigated by repeating the experiments and comparing the crack responses to the value of the edge effect. The sensor axis was parallel to the axis of the tube specimen (z direction). 50 kHz excitation frequency was used.

The OD 10% (127 μm) and OD 20% (254 μm) deep cracks were detected by the probe. The measured results of the single line scan can be seen in Fig. 24(a) and 24(b), for the same axial cracks, at different magnification. The peak marked with "A_0" belongs to an "unofficial," previously not identified minor crack, which is independent of the edge effect.

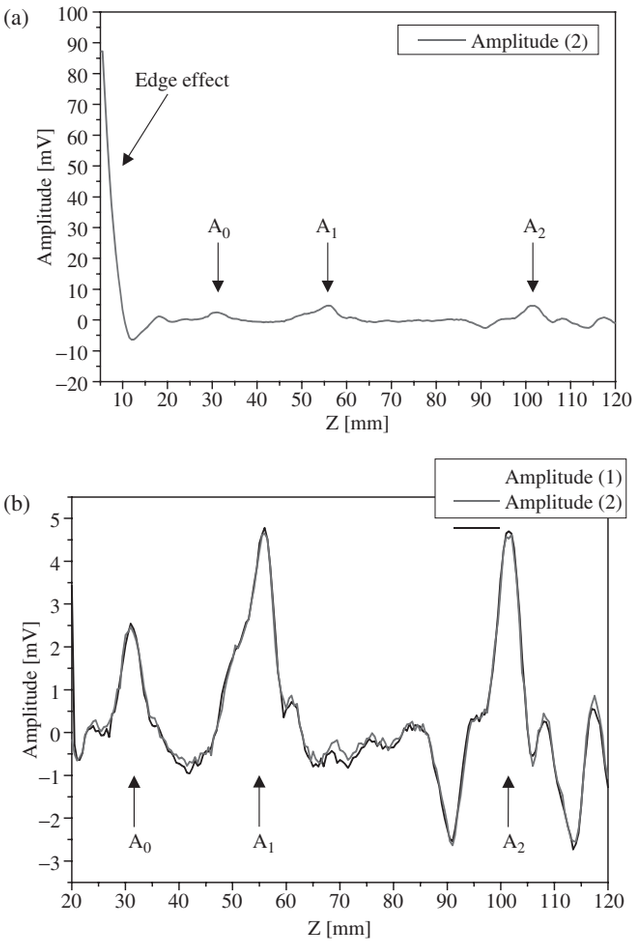

Figure 24. Single line scan result of OD 10% (A_1) and OD 20% (A_2) 5 mm long axial EDM crack detection in INCONEL 600 tube, at different magnification. Reprinted with permission from [153], A. Gasparics, et al., in "Electromagnetic Nondestructive Evaluation (V)" (J. Pávó, G. Vértesy, T. Takagi, and S. S. Udpa, Eds.), p. 317. IOS Press, 2001. © 2001, IOS Press.

The line scan was repeated in order to be able to separate the systematic (position dependent) noise and the non-systematic (time dependent) noise. The signal to noise ratio (S/N) was determined by the peak to peak value of the recorded response magnitude and the ratio of the time-dependent noise (the standard deviation of the difference of the two curves). We got 26 dB value for the OD 10% and 28 dB for the OD 20% crack.

The single line scan for circumferential cracks is shown in Fig. 25. It should be noted that there is no axial (z) component of the perturbed magnetic field when the Fluxset probe is exactly over the circumferential crack. Therefore two peaks of the response magnitude are expected during the line scan: when both the exciting coil and the stream of the eddy currents touch the crack area and when they leave it. This difference between the axial and circumferential type crack detection allows to recognize the orientation of the flaw.

d. Simultaneous Detection of ac and dc Magnetic Fields The sensitivity of the applied Fluxset sensor is practically independent of the measured field frequency in its operational range from 200 kHz down to dc. This means that the Fluxset probe can simultaneously measure different frequency ac magnetic field perturbations and the constant magnetic field with the same sensitivity. Interesting results were obtained during the inspection of the natural cracks, stress corrosion cracks (SCC) and intergranular attacking (IGA) in tubes made of INCONEL 600.

The mean value of the Fluxset sensor output is proportional to the actual dc field. The axial magnetic field amplitude map over the surface of a tube having natural cracks can be seen in Fig. 26. Performing the eddy current measurement, the response of the natural crack can be found in the center of Fig. 26(a), but much larger signal can also be observed in the surface scan, which is attributed to the existence of strong dc magnetic field. There was no

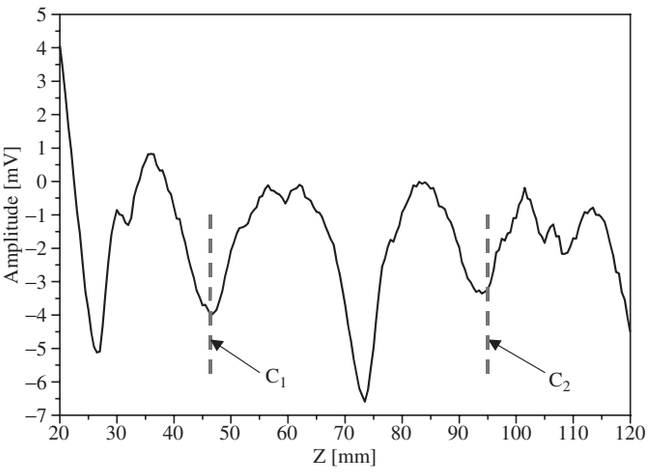

Figure 25. Single line scan result of OD 10% (C_1) and OD 20% (C_2) 5 mm long circumferential EDM crack detection in INCONEL 600 tube. Reprinted with permission from [153], A. Gasparics, et al., in "Electromagnetic Nondestructive Evaluation (V)" (J. Pávó, G. Vértesy, T. Takagi, and S. S. Udpa, Eds.), p. 317. IOS Press, 2001. © 2001, IOS Press.

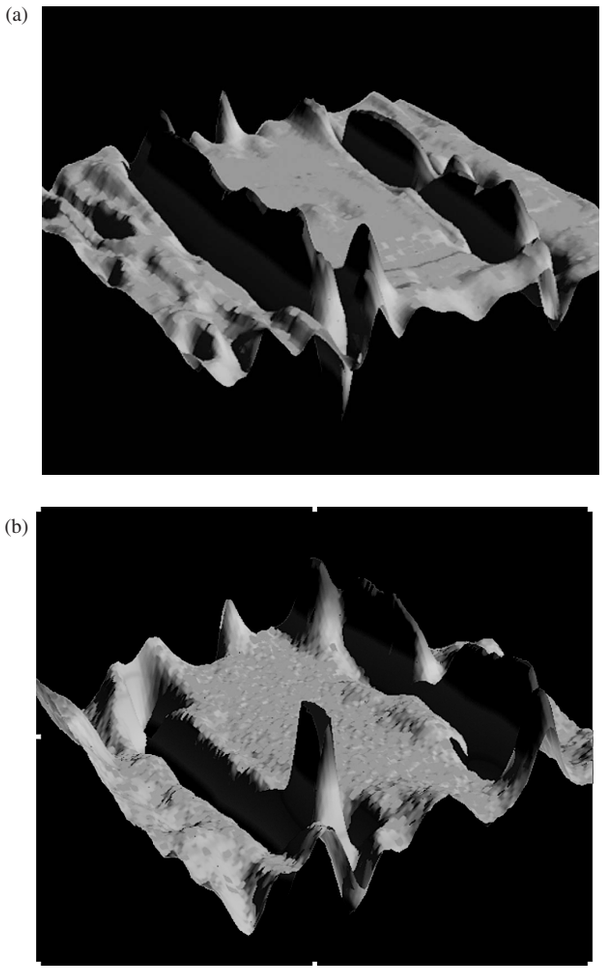

Figure 26. The axial magnetic field amplitude map over the surface of a tube having natural cracks. (a) 50 kHz, (b) 0 Hz (dc case). Reprinted with permission from [153], A. Gasparics, et al., in "Electromagnetic Nondestructive Evaluation (V)" (J. Pávó, G. Vértesy, T. Takagi, and S. S. Udpa, Eds.), p. 317. IOS Press, 2001. © 2001, IOS Press.

low frequency field feedback applied in the experiment and the variation of the dc field was strong enough to saturate the measuring system. The measured field pattern, without ac excitation (simple dc field measurement) is shown in Fig. 26(b). The influence of the dc magnetic field pattern on the eddy current measurement can be observed by comparing Fig. 26(a) and 26(b).

We found that all of the specimens with natural SCC or IGA type cracks have own magnetic moment, in spite of the fact, that original INCONEL 600 samples are not ferromagnetic. The observed dc B field variation can be caused by the interaction between the magnetic specimen and the Earth's magnetic field, for instance. The magnetic property could be assigned to the effect of the corrosion, to the surface dust or to some other influence of the special treatment, which was applied in order to prepare these artificial flaws. If that part of the tube, which has acquired this magnetic property, is not concentrated only on the surface it can have a strong influence on the eddy current distribution inside the tube wall. Therefore these specimens should be considered as being composed of non-homogenous and non-linear magnetic material.

This latter measurement result calls attention to an additional possible advantage of the Fluxset type ECT measurement technique, namely that the modification of eddy currents and the induced changes in the magnetic moment of the investigated sample can be monitored simultaneously.

e. Crack Detection in Aluminum Rivet Joints Fast and reliable inspection of lap-joints for minute cracks deeply buried beneath rivet heads is an important issue of the aircraft maintenance process. For solving this problem, Fluxset type eddy current probe was applied for detection and reconstruction of small cracks hidden under rivet heads [155–157]. The work mainly focused on the second-layer cracks in riveted aluminum-to-aluminum structures. Experimental data were compared with results of numerical simulation in order to asses the possibility of solving the inverse problem. The samples represent aluminum-to-aluminum double layer sandwiches with fastener holes and inserted rivets. Figure 27 shows schematically the sample geometry together with the ECT probe.

The probe made a part of automated system for nondestructive evaluation of riveted aluminum joints. The improvement of the probe concerned more distinct discrimination of the signals due to a subsurface crack and a fastener hole. Besides the innovative eddy-current probe the system featured a computational tool aimed both at computer-aided electromagnetic design of eddy current probes and quantitative reconstruction of detected defects. The approach adopted for defect reconstruction was of phenomenological nature, which provided a valuable tool for comprehensive understanding of behavior of the inspection set-up and probes development. The numerical technique was based on the edge element integral formulation of the eddy current problem and offered fast and accurate numerical modeling.

The experimental data exhibited favorable agreement with numerical simulations, which is illustrated in Fig. 28. This allows us to be confident about the possibility of solving the inverse problem.

f. Measurement of Insulation Layer Thickness Based on Fluxset type ECT probe, a new measurement method

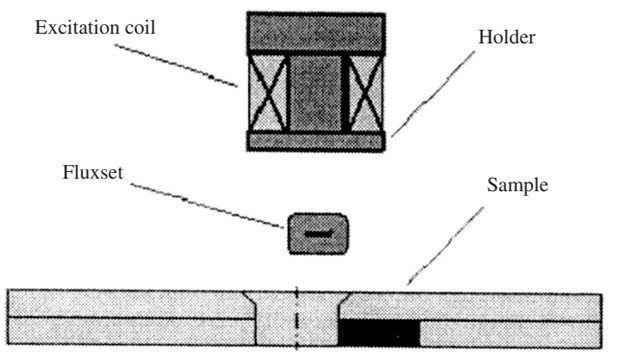

Figure 27. ECT probe and geometry of aluminum-to-aluminum double layer sandwiches with fastener hole and inserted rivet. Reprinted with permission from [156], M. Morozov, et al., in "Electromagnetic Nondestructive Evaluation (VIII)" (T. Sollier, D. Prémel, and D. Lesselier, Eds.), p. 207. IOS Press, Amsterdam, 2004. © 2004, IOS Press.

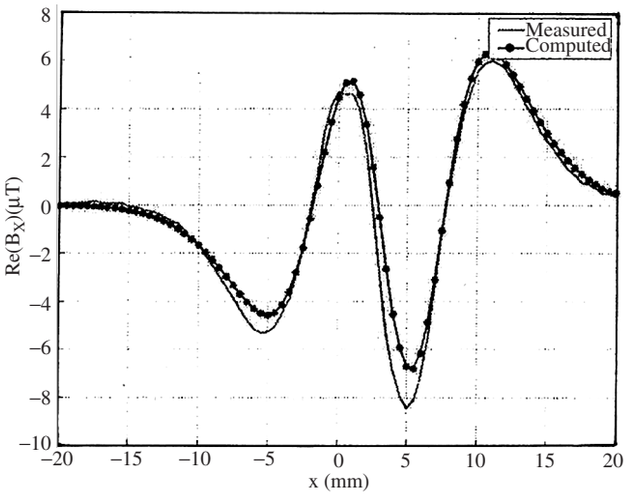

Figure 28. Crack contribution of the response to an ID 100% 5 mm long crack in the 2nd layer originating from a fastener hole with rivet, measurement vs. simulation, real component (after [155]). Reprinted with permission from [156], M. Morozov, et al., in "Electromagnetic Nondestructive Evaluation (VIII)" (T. Sollier, D. Prémel, and D. Lesselier, Eds.), p. 207. IOS Press, Amsterdam, 2004. © 2004, IOS Press.

has been developed for the determination of the insulation layers' thickness, which cover the surface of conductive specimens [158]. The traditional inductive coil based method is excellent up to some millimeters of the thickness, however, it is not possible to determine the thickness of thick (above 10 mm) layers by these devices, which is an important task in certain fields of application. The other drawback of these devices that they can hardly handle the probe tilting error, which often happens if the surface is rough.

The exciting coil of the ECT probe is used for generating ac electromagnetic field in the conductive material. This way the insulation layer is considered as a lift-off of the probe from the conductive surface. Between the sample and the exciting coil the magnetic field sensor placed. If the sensor is properly balanced, it measures only the axial component of the magnetic field, it is not sensitive to the perpendicular field. However, in this application, the sensor is not balanced exactly into the center position of the exciting coil. Therefore it measures the exciting field of the coil, too. This field is the result of the interaction between exciting coil and the conductive specimen. The specimen reflects the exciting field and modifies the field distribution around the exciting coil. The degree of this field modification depends on the distance between the coil and the specimen surface. As a consequence, the magnetic field detected by the Fluxset sensor depends on this distance as well.

By applying this method, insulation layer thickness up to 20 mm can be measured with good signal/noise ratio. Within the 0–5 mm lift-off range the reachable precision of the thickness measurement is ∼0.12%. The signal to noise ratio (of the whole signal processing chain) was better than 89 dB, which results better than 10^{-4} thickness resolution. It is also capable to take into account the probe tilting and the measurement process is fast enough. The measured change of the output voltage of the ECT probe as a function of the lift-off distance is shown in Fig. 29.

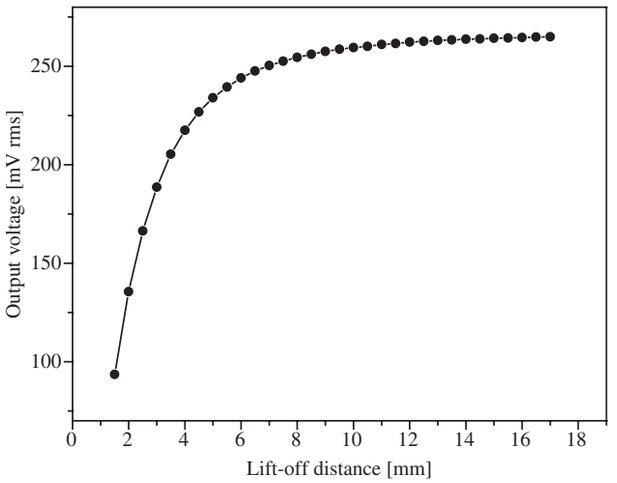

Figure 29. The measured change of the output voltage of the device as a function of the lift-off distance.

4.2. Magnetic Flux Leakage Measurements

4.2.1. Nondestructive Characterization of Plastically Deformed Steel Plates

Among the several nondestructive evaluation methods, magnetic flux leakage measurement is one of the most promising approaches for inspection of iron based, ferromagnetic materials [159]. Various methods of nondestructive evaluation for iron based materials have been investigated by several authors by observing ultrasonic propagation, X-ray methods, magnetic noise measurements [160], etc. Recently, by using AMR, SQUID and Hall devices, the magnetic leakage flux of strained samples has been intensively investigated [161–164].

The microstructure of the steel has influence on the local magnetic properties. This fact gives an opportunity to try to detect the presence of the degradation by sensing the changes of the magnetic properties of the investigated specimen [165]. The local variation of the magnetic behavior of the material effects the magnetic distribution, both inside and outside of the sample. This well-known principle of leakage flux testing is based on the magnetic field mapping over the specimen surface. The magnetic field sensor, applied for this purpose, must have high sensitivity, high spatial resolution and it should be suitable for the detection of the magnetic field direction as well. The Fluxset sensor fulfills these demands. The main goal in this step was not to analyze the influence of the strain on the sample structure but rather to demonstrate the efficiency of the proposed technique.

Measurements were performed on low alloy steel (A533B) plate samples. This is the material of pressure wessels. The A533B steel is composed of Fe, Mn, Ni, Mo and C with total impurities less than 3 Wt%. The specimen was in a standard tensile test sample as shown in Fig. 30. The thickness of the specimen is 2 mm. Monotonically increased tensile stress up to $P = 529$ MPa was applied on this sample. The sample was polarized in 1 kOe magnetic field prior to the measurement and magnetically it was in remanent state.

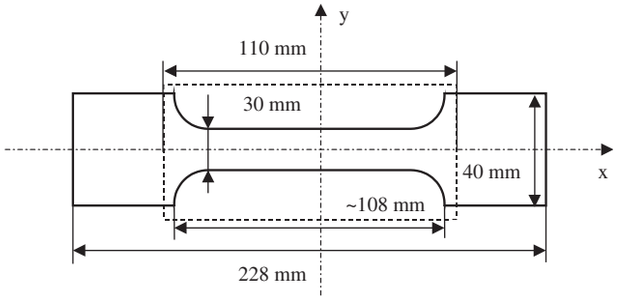

Figure 30. The shape and sizes of the measured sample and the investigated area. Reprinted with permission from [151], G. Vértesy and A. Gasparics, *Mat. Sci. Forum* 414, 343 (2003). © 2003, Trans. Tech. Publications.

The measurement of the flux leakage was performed in zero external field by applying sensor orientations parallel and normal to the sample surface. Two dimensional magnetic field patterns over the surface of plastically deformed A533B type steel plate specimens were recorded. The Fluxset sensor is especially suitable for the detection of the surface parallel components (x and y) of the field, which are more relevant than the surface perpendicular (z) component in case of the leaking and returning flux lines. The leakage flux density, measured by a sensor oriented in x direction, scanning over the surface is shown in Fig. 31. (Only the area of the specimen, indicated in Fig. 30, was measured.)

The applied Fluxset type sensor had 5 mm long core material—that was the largest dimension of the sensor. The spatial resolution is more than hundred times better than the length of the applied core (5 mm) that means the attainable spatial resolution is better than 50 μm. 500 μs acquisition time was applied for each point scanned. This acquisition time can be reduced to 10 μs due to the operational principle of the sensor and the applied driving frequency. The maximum of the attainable scanning speed can be calculated from the required spatial resolution (Δs) and the acquisition time (Δt), which was 1 m/s in the described measurement and which is 50 m/s in case of $\Delta t = 10$ μs, $\Delta s = 0.5$ mm.

Significant differences can be observed between the affected and the untouched sample (not shown here) both in the x and in the y magnetic field pattern. The obtained field map is the result of three phenomena: it is effected by the geometry, it is influenced by the residual stresses (if there are any) and also by the microstructural changes in the material. The observed parallel lines are supposed to correspond to the bands produced during the plastic slip deformation.

Figure 31. X component of the leakage flux density of plastically deformed A533B type steel plate specimen, measured with $\Delta x = \Delta y = 0.5$ mm step resolution and $\Delta t = 500$ μs acquisition time. Reprinted with permission from [151], G. Vértesy and A. Gasparics, *Mat. Sci. Forum* 414, 343 (2003). © 2003, Trans. Tech. Publications.

Samples, having small remanence, can also be measured by this technique, so the previous magnetization of the samples is not necessary. Last, but not least, the described technique is suitable for the simultaneous measurement of the dc magnetic leakage field and the ac magnetic field of the eddy currents, which allows to obtain more information about the defects and the degradation of the material.

4.2.2. Measurement of Magnetic Flux Density Electrolyte–Metal Interface

On of the newest application of Fluxset sensor is described in [166]. In this work a novel experiment for characterization of liquid-solid interface deformation by measurement of magnetic field density has been carried out. A single-axis Fluxset sensor has been used to measure the distribution of radial and z-components of magnetic field around a rotating cylindrical cell containing a solid copper cylinder with a sinusoidal surface and KOH solution above it. The signal from the magnetic sensor has been collected by a data acquisition board and processed by fast Fourier transformation. The experimental results agree well with the theoretical predictions calculated by the finite element method, which reveal that the set-up is applicable to develop magnetic field tomography for reconstruction of interface deformation.

5. CONCLUSION

A new type of magnetic field sensor, which belongs to the family of pulse-position type fluxgate sensors, has recently been developed, and complete investigation of the device has been performed. The results show that this type of sensor has reached the parameters usual for low-noise and long term stable magnetometers based on the conventional second-harmonic principle of fluxgate magnetometers. In certain fields (simple construction, wide temperature range of operation, higher frequency limit, price) it can be even better than conventional fluxgates.

The application possibilities of the sensor has been sketched, emphasizing and illustrating by experimental results its application in nondestructive material testing, which is considered to be one of the most promising field of applications of this device.

The most important achievements are related to the design of an innovative eddy current probe for NDT applications and to the development of several numerical methods and tools for improving the detection of defects and material inhomogeneities. The performance of the Fluxset probe (in terms of signal to noise ratio, spatial resolution and depth sensitivity) has been found to be comparable and often better than the existing alternative probes. This is due to the high sensitivity and to the frequency independent behavior of the Fluxset sensor, which make possible the detection of defects, located deeply in the material. The measurements have shown also the other advantageous feature of this method, that the dc magnetic field can be simultaneously detected during the measurements, which can also give

important information about the condition of some specimens. Evaluating the results of eddy current measurements, experimental data have exhibited favorable agreement with numerical simulations, which is an important step towards solving the inverse problem.

Fluxset sensor is believed to be very suitable for miniaturization, due to its simple construction.

GLOSSARY

Amorphous metals They are alloys, mainly based on iron and cobalt, rapidly solidified from melt. They exhibit a topological disorder without crystalline structure. A typical production process is melt spinning of thin wires and ribbons.

Anisotropic magnetoresistance (AMR) This effect appears in ferro- and ferrimagnetic thin films with uniform orientation of the spontaneous magnetization that is parallel to the easy axis of minimum uniaxial anisotropy energy in the absence of an applied field.

Boundary Integral Method Computational technique, where the solution of partial differential equations is thought via the solution of an integral equation. The unknown quantity is usually a function understood on the boundary of the modeled object.

Coercive force, or coercivity The reverse magnetic field, required to reduce the magnetic induction to zero from being saturated previously by the opposite direction magnetic field.

Eddy current If a conducting material is subjected to an alternating magnetic field then electromagnetic fields are induced in the material, which cause eddy currents to circulate in the material because of resistive property of it. These eddy currents produce a secondary magnetic field in the material.

Finite element method Computational technique, which is usually used for the solution of partial differential equations. The whole computational domain is discretized by a finite mesh. The unknown functions (usually some potential functions) are approximated on this mesh and their actual values are obtained by the minimization of a functional.

Hall effect It refers to the setting up of a transverse electric field and potential difference in a metal or semiconductor conducting an electric current if it is put into a magnetic field perpendicular to the direction of the current.

Hyteresis loop A curve showing the change in magnetic induction of a ferromagnetic body to which an external field is applied as the intensity of this field is varied (B(H) loop).

Magnetostriction The magnetization of a ferromagnetic material is in nearly all cases accompanied by changes in dimensions. The resulting strain is called the magnetostriction λ.

Initial permeability It is represented by the tangential line on B(H) curve at the origin.

Saturation magnetization Application of a magnetic field causes the magnetic induction to increase in the field direction. If the field increased indefinitely the magnetization eventually reaches saturation at a value, which we shall designate as saturation magnetization. This represents a condition where all the magnetic dipoles within the material are aligned in the direction of magnetic field.

Superconducting Quantum Interference Devices (SQUIDs) The most sensitive magnetic sensors. Operation of these sensors is based upon the properties of the superconducting state—namely, flux quantization and the Josephson effect.

ACKNOWLEDGMENTS

The author is indebted to A. Gasparics and J. Szöllõsy for their work in the Fluxset sensor development and to A. Körmendi (Eötvös Loránd Geophysical Institute of Hungary, Geophysical Observatory, Tihany) for the reference measurements of the sensor.

REFERENCES

1. D. I. Gordon, R. H. Lundsten, and R. A. Chiarodo, *IEEE Trans. Magn*. 1, 330 (1965).
2. V. Vacquier, *Rev. Sci. Instrum.* 18, 483 (1947).
3. Technical Specification, "Static 3 Axis Magnetometer Doc"—Ref. 34114, Crouzet.
4. R. D. Wyckoff, *Geophysics* 13, 182 (1948).
5. L. G. Lawrence, *Elektronik* 11, 323 (1964).
6. S. V. Marshall, *IEEE Trans. Magn.* 7, 183 (1971).
7. S. Takeuchi and H. Harada, *IEEE Trans. Magn.* 20, 1723 (1984).
8. D. Son, *IEEE Trans. Magn.* 25, 3420 (1989).
9. T. Sonoda and R. Ueda, *IEEE Trans. Magn.* 25, 3393 (1989).
10. P. A. Robertson, *Electr. Lett.* 33, 396 (1997).
11. P. A. Robertson, "Proc. Sensor & Transducer Conf," p. 28. Birmingham, UK, 1999.
12. D. Praslicka, *IEEE Trans. Magn.* 30, 934 (1994).
13. P. D. Dimitropoulos and J. N. Avarisiotis, *Sensors and Actuators A* 94, 165 (2001).
14. F. Primdahl, P. Ripka, J. R. Petersen, and O. V. Nielsen, *Meas. Sci. Tecnol.* 2, 1039 (1991).
15. F. Primdahl, *Publications of the Earth Physics Branch* 41, 1 (1970).
16. P. H. Serson and F. Primdahl, *Publications of the Earth Physics Branch* 43, 8 (1972).
17. F. Primdahl and R. L. Coles, *Adv. Space Res.* 8, 79 (1988).
18. H. P. Thomas, U.S. Patent No. 2,016,977, 1935.
19. H. Aschebrenner and G. Goubau, *Hochfrequenztechnik und Elektroakustik* 47, 177 (1936).
20. W. A. Geyger, "Magnetic-amplifier Circuits." McGraw-Hill, New York, 1957.
21. P. Dyal and D. Gordon, *IEEE Trans. Magn.* 9, 226 (1973).
22. F. M. Neubauer, *Space Sci. Rev.* 23, 250 (1988).
23. W. F. Stuart, *Reports on Progress in Physics* 23, 250 (1972).
24. E. R. Niblett and R. L. Coles, "Proc. Int. Workshop on Magnetic Observatory Instruments," p. 11, Ottawa, Canada, 1988.
25. D. I. Gordon and R. E. Brown, *IEEE Trans. Magn.* 8, 76 (1972).
26. F. Primdahl, *J. Phys. E: Sci. Instrum.* 12, 241 (1979).
27. N. N. Kolachewski, "Fluctuation Processes in Ferromagnetic Materials." Nauka, Moscow, Russia, 1985.
28. Ju. V. Afanasiev, "Ferroprobes," Energia, Moscow, Russia, 1969.
29. T. Saito, "Onagawa Magnetic Observatory," Tohoku University, Sendai, Japan, 1980.
30. W. Bornhöfft and G. Trenkler, "Magnetic Sensors" (R. Boll and K. J. Overshott, Eds.), Vol. 5, p. 153. VCH, Veiden, Germany, 1989.
31. O. V. Nielsen, J. R. Petersen, F. Primdahl, P. Brauer, B. Hernando, and A. Fernandez, *Meas. Sci. Technol.* 6, 1099 (1995).
32. "Fluxgate Magnetometry," pp. 726–732. Electronic World, Sept. 1991.

33. P. Ripka, *Sensors and Actuators A* 33, 129 (1992).
34. P. Ripka, *Sensors and Actuators A* 8, 106 (2003).
35. P. Ripka, *J. Magn. Magn. Mater.* 215–216, 735 (2001).
36. P. Ripka, "Magnetic Sensors and Magnetometers." Artech House, Boston, London, 2001.
37. D. Robbes, C. Dolabdijan, S. Saez, Y. Monfort, G. Kaiser, and P. Ciureanu, *IEEE Trans. Appl. Supercond.* 11, 629 (2001).
38. P. Ripka and G. Vértesy, *J. Magn. Magn. Mater.* 215–216, 795 (2000).
39. M. R. J. Gibbs and P. T. Squire, "Magnetic Sensors" (R. Boll and K. J. Overshott, Eds.), Vol. 5, p. 447. VCH, Veiden, Germany, 1989.
40. M. H. Acuna, *IEEE Trans. Magn.* 10, 519 (1974).
41. D. J. Southwood, W. A. C. Mier-Jedrzejowicz, and C. T. Russel, *IEEE Trans. Geosci.* 23, 301 (1985).
42. M. H. Acuna, *Rev. Sci. Instrum.* 73, 3717 (2002).
43. F. M. Neubauer, *Space Sci. Rev.* 23, 250 (1988).
44. R. Langel, G. Ousley, J. Berbert, J, Murphy, and M. Settle, *Geophys. Res. Lett.* 9, 243 (1982).
45. R. L. Coles, Ed., "Proc. Int. Workshop on Magnetic Observatory Instruments," Ottawa, Canada, 1986.
46. K. Kauristie, C. Sucksdorff, and H. Nevanlinna, "Proc. Int. Workshop on Geomagnetic Observatory Data Acquisition and Processing," Nurmijarvi, Finland, 1990.
47. L. V. Medford, C. G. MacLennan, P. E. Rosenfeld, L. J. Lanzerotti, and M. H. Acuna, *IEEE Trans. Geophys.* 19, 122 (1981).
48. A. White, *Marine Geophys. Res.* 4, 105 (1979).
49. A. J. Clarc, *Geophys.* 51, 1404 (1986).
50. M. Kono, Y. Hamano, T. Nishitani, and T. Tosha, *Geophys. J. R. Astron. Soc.* 67, 217 (1981).
51. T. Seitz, *Sensors and Actuators A*, 21–23, 799 (1990).
52. D. C. Lewis and H. Ormondroyd, *Mining Technol.* June, 220 (1978).
53. B. G. Steward, J. A. Rollo, and J. F. L. Simmons, *J. Phys. E: Sci. Instrum.* 22, 457 (1989).
54. J. F. Scarzello and G. W. Usher, *IEEE Trans. Magn.* 13, 1101 (1977).
55. T. J. Peters, *IEEE Trans. Veh. Technol.* 35, 41 (1986).
56. W. H. Campbell and J. E. Zimmermann, *IEEE Trans. Geosci.* 18, 244 (1980).
57. W. J. Moore and P. N. Miljanic, "The Current Comparator." UK, Peter Peregrimus, IEE, London, 1988.
58. P. Ripka and P. Navratil, *Sensors and Actuators A* 60, 76 (1997).
59. J. M. G. Merayo, J. R. Petersen, O. V. Nielsen, F. Primdahl, and P. Brauer, *Sensors and Actuators A* 93, 185 (2001).
60. J. M. G. Merayo, P. Brauer, and F. Primdahl, "Proc. Eurosensors XVI Conf.," Prague, Czech Republic, 2002.
61. D. Jiles, "Introduction to Magnetism and Magnetic Materials." Chapman & Hall, London, 1998.
62. F. Förster, *Nondestructive Test.* 13, 31 (1955).
63. H. Grüger, *Sensors and Actuators A*, 106, 326 (2003).
64. C. Carr and J. Macfarlene, *Insight* 41, 20 (1999).
65. P. Ripka, M. Vopálensky, A. Platil, M. Döscher, K. M. H. Lenssen, and H. Hauser, *J. Magn. Magn. Mater.* 254–255, 639 (2003).
66. M. Vopálensky, P. Ripka, and A. Platil, *Sensors and Actuators A* 110, 182 (2003).
67. M. Vopálensky, P. Ripka, and A. Platil, *Sensors and Actuators A* 106, 38 (2003).
68. S. K. Ghatak and A. Mitra, *J. Magn. Magn. Mater.* 103, 85 (1992).
69. P. Ripka, S. O. Choi, S. Kawahito, A. Tipek, and M. Ishida, *Sensors and Actuators A* 91, 65 (2001).
70. P. Ripka, S. O. Choi, A. Tipek, S. Kawahito, and M. Ishida, *Sensors and Actuators A* 92, 30 (2001).
71. P. Ripka, S. O. Choi, A. Tipek, S. Kawahito, and M. Ishida, *IEEE Trans. Magn.* 37, 1998 (2002).
72. P. Kejik, L. Chiesi, B. Janossy, and R. S. Popovic, *Sensors and Actuators A* 81, 180 (2000).
73. Siemens, "Magnetic Sensors," Brochure, 1998.
74. O. V. Nielsen, B. Hernando, J. R. Petersen, and F. Primdahl, *J. Magn. Magn. Mater.* 83, 405 (1990).
75. O. Dezuari, E. Belloy, S. E. Gilbert, and M. A. M. Gijs, *Sensors and Actuators A* 81, 200 (2000).
76. E. Belloy, S. E. Gilbert, O. Dezuari, M. Sancho, and M. A. M. Gijs, *Sensors and Actuators A* 85, 304 (2000).
77. S. O. Choi, S. Kawahito, K. Takahashi, Y. Matsumoto, M. Ishida, and Y. Tadokoro, *Sensors and Materials* 9, 241 (1997).
78. M. Schneider, "Proc. IEDM Conf. IEEE," 36.5.1, 1997.
79. P. M. Drljaca, P. Kejik, F. Vincent, D. Piguet, F. Gueissaz, and R. S. Popovic, "Proc. Eurosensors XVI. Conf.," Prague, Czech Republic, 2002.
80. S. Kawahito, H. Satoh, M. Sutoh, and Y. Tadokoro, *Sensors and Actuators A* 54, 612 (1996).
81. R. Gottfried, *Sensors and Actuators A* 54, 443 (1996).
82. T. M. Liakopoulos and C. H. Ahn, *Sensors and Actuators A* 77, 66 (1999).
83. R. A. Rub, S. Gupta, and C. H. Ahn, "Proc. Transducers 2001 at Eurosensors XV. Conf.," Munich, Germany, 2001.
84. K. Kuchenbrand, D. Huhnke, K. Lauckner, and M. Schilling, "Proc. Eurosensors XVI. Conf.," Prague, Czech Republic, 2002.
85. L. Chiesi, P. Kejik, B. Janossy, and R. S. Popovic, *Sensors and Actuators A* 82, 174 (2000).
86. P. M. Drljaca, P. Kejik, F. Vincent, D. Piguet, F. Gueissaz, and R. S. Popovic, *Sensors and Actuators A* 110, 236 (2004).
87. F. Primdahl, B. Hernando, J. R. Petersen, and O. V. Nielsen, *Meas. Sci. Technol.* 5, 359 (1994).
88. H. Auster, *Meas. Sci. Technol.* 6, 477 (1995).
89. E. B. Pedersen, F. Primdahl, J. R. Petersen, J. M. G. Merayo, P. Brauer, and O. V. Nielsen, *Meas. Sci. Technol.* 10, N124 (1999).
90. S. Kawahito, "Transducers Conf.," Sendai, Japan, 1999.
91. S. Koga, *Trans. IEE of Japan* 117E, 84 (1997).
92. S. Striker, *Trans. IEE (I)* 80, 253 (1961).
93. G. Trenkler, *Meβtechnik* 78(10), 205–209.
94. W. Heinecke, *Technisches Messen* 48, 6 (1981).
95. M. H. Rhodes, Magnetic Field Detection by Differential Phase Lag, U.S. Patent 4,321,536, March, 1982.
96. K. Weyand and V. Bosse, *IEEE Trans. Magn.* 46, 617 (1997).
97. G. Vértesy, A. Gasparics, and J. Szöllösy, *Sensors and Actuators A* 85, 202 (2000).
98. D. Ioan, F. I. Hantila, M. Rebican, and D. Constantin, in "Electromagnetic Nondestructive Evaluation (II)" (R. Albanese, G. Rubinacci, T. Takagi, and S. S. Udpa, Eds.), p. 160. IOS Press, Amsterdam, 1998.
99. R. Albanese, A. Formisano, R. Fresa, and G. Rubinacci, in "Electromagnetic Nondestructive Evaluation (II)" (R. Albanese, G. Rubinacci, T. Takagi, and S. S. Udpa, Eds.), p. 180. IOS Press, Amsterdam, 1998.
100. D. Ioan, M. Rebican, G. Ciuprina, and P. Leonard, in "Electromagnetic Nondestructive Evaluation (II)" (R. Albanese, G. Rubinacci, T. Takagi, and S. S. Udpa, Eds.), p. 152. IOS Press, Amsterdam, 1998.
101. A. Bernieri, G. Betta, G. Rubinacci, and F. Villone, "Proc. of IMTC Conference," Venice, Italy, 1999.
102. K. Preis, I. Bardi, O. Biro, K. R. Richter, J. Pávó, A. Gasparics, and I. Ticar, *IEEE Trans. Magn.* 34, 3475 (1998).
103. D. Rodger and P.K. Vong, in "Electromagnetic Nondestructive Evaluation (III)" (D. Lesselier and A. Razek, Eds.), p. 182, IOS Press, Amsterdam, 1999.
104. R. Albanese, M. Federico, A. Formisano, R. Fresa, and G. Rubinacci, in "Electromagnetic Nondestructive Evaluation (III)" (D. Lesselier and A. Razek, Eds.), p. 3, IOS Press, Amsterdam, 1999.

105. R. Albanese, F. I. Hantila, and G. Rubinacci, *IEEE Trans. Magn.* 32, 784 (1996).
106. R. Albanese and G. Rubinacci, *Advances in Imaging and Electron Physics* 102, 1 (1998).
107. R. Albanese, A. Formisano, G. Rubinacci, and R. Fresa, in "Electromagnetic Nondestructive Evaluation (II)" (R. Albanese, G. Rubinacci, T. Takagi, and S. S. Udpa, Eds.), p. 180. IOS Press, Amsterdam, 1998.
108. D. Ioan, M. Rebican, and M. Iordache, in "Electromagnetic Nondestructive Evaluation (II)" (R. Albanese, G. Rubinacci, T. Takagi, and S. S. Udpa, Eds.), p. 120. IOS Press, Amsterdam, 1998.
109. D. Ioan, I. Munteanu, and C.G. Constantin, *IEEE Trans. Magn.* 34, 548 (1998).
110. D. Ioan, A. Formisano, A. Gasparics, I. Munteanu, and M. Rebican, in "Electromagnetic Nondestructive Evaluation (III)" (D. Lesselier and A. Razek, Eds.), p. 14. IOS Press, Amsterdam, 1999.
111. D. Ioan, I. F. Hantila, M. Rebican, and C. Constantin, in "Electromagnetic Nondestructive Evaluation (II)" (R. Albanese, G. Rubinacci, T. Takagi, and S. S. Udpa, Eds.), p. 160. IOS Press, Amsterdam, 1998.
112. R. Albanese, G. Rubinacci, A. Tamburrino, and F. Villone, in "Non-Linear Electromagnetic System" (P. Di Barba and A. Savini, Eds.). IOS Press, Amsterdam, 2000.
113. A. Bernieri, G. Betta, G. Rubinacci, and F. Villone, *IEEE Trans. on Instrumentation and Measurements* 49, 455 (2000).
114. D. C. Scouten, *IEEE Trans. Mag.* 8, 223 (1972).
115. F. E. Luborsky, "Amorphous Metallic Alloys." Butterworths, London, 1983.
116. K. Moorjani and J.M.D. Coey, "Magnetic Glasses." Elsevier, Amsterdam, 1984.
117. H. K. Lachowicz, *Journal of Technical Physics*, XLII, 127 (2001).
118. K. Mohri, *IEEE Trans. Mag.* 20, 942 (1984).
119. K. Shirae, *IEEE Trans. Mag.* 20, 1299 (1984).
120. G. Vértesy, A. Gasparics, and Z. Vértesy, *J. Magn. Magn. Mater.* 196–197, 333 (1999).
121. G. Vértesy, A. Gasparics, Z. Vértesy, and E. Tóth-Kádár, *J. Magn. Magn. Mater.* 215–216, 762 (2000).
122. G. Bordin, G. Buttino, A. Cecchetti, and M. Poppi, *J. Magn. Magn. Mater*. 133, 259 (1994).
123. M. Pardavi-Horváth and H. Kim, *J. Korean Magn. Soc.* 5, 663 (1995).
124. R. Albanese, A. Bossavit, R. Fresa, D. Ioan, G. Rubinacci, A. Tamburrino, and F. Villone, *Physica B—Condensed Mater* 275, 228 (2000).
125. D. Ioan, I. Munteanu, and C. Popeea, *COMPEL* 18, 515 (1999).
126. D. Ioan, M. Rebican, and A. Gasparics, *COMPEL* 18, 469 (1999).
127. G. Vértesy and A. Gasparics, *J. Electrical Engineering* 53, 53 (2002).
128. J. Pávó, *ACES Journal*, 12, 3237 (1997).
129. J. Pávó, D. Ioan, P. Novotny, A. Razek, K. Richter, G. Rubinacci, D. Rodger, and G. Vértesy, in "Non-Linear Electromagnetic System" (P. Di Barba and A. Savini, Eds.), p. 94. IOS Press, Amsterdam, 2000.
130. J. Pávó, M. Uesaka, and K. Miya, in "Review of Progress in Quantitative Nondestructive Evaluation" (D. O. Thompson and D. E. Chimenti, Eds.) Vol. 13, p. 919. Plenum Press, New York, 1994.
131. J. Pávó and K. Miya, *IEEE Trans. Magn.* 32, 1597 (1996).
132. J. Pávó and K. Miya, *IEEE Trans. Magn.* 30, 3407 (1994).
133. R. Albanese, G. Rubinacci, A. Tamburrino, and F. Villone, *Int. J. Appl. Electrom.* 12, 115 (2000).
134. A. Gasparics, Cs. S. Daróczi, G. Vértesy, J. Pávó, in "Electromagnetic Nondestructive Evaluation (II)" (R. Albanese, G. Rubinacci, T. Takagi, and S. S. Udpa, Eds.), p. 160. IOS Press, Amsterdam, 1998.
135. R. Albanese, G. Rubinacci, and F. Villone, in "Electromagnetic Nondestructive Evaluation (IV)" (S. S. Udpa, T. Takagi, J. Pavo, and R. Albanese, Eds.), p. 58. IOS Press, Amsterdam, 2000.
136. R. Albanese, G. Rubinacci, and F. Villone, *J. Comp. Phys.* 152, 736 (1999).
137. R. Albanese, R. Barresi, M. Carbone, and A. Gasparics, in "Electromagnetic Nondestructive Evaluation (VIII)" (T. Sollier, D. Premel, and D. Lesselier, Eds.), p. 52. IOS Press, Amsterdam, 2004.
138. C. V. Dodd and W. E. Deeds, *J. Appl. Phys.* 39, 2829 (1968).
139. J. Pávó, A. Gasparics, I. Sebestyén, and G. Vértesy, *Sensors and Actuators A* 110, 105 (2004).
140. J. Pávó and A. Gasparics, *COMPEL* 18, 436 (1999).
141. O. Bíró, K. Hollaus, J. Pávó, and K. Preis, in "Electromagnetic Nondestructive Evaluation (V)" (J. Pávó, G. Vértesy, T. Takagi, and S. S. Udpa, Eds.), p. 11. IOS Press, Amsterdam, 2001.
142. J. Pávó, in "Electromagnetic Nondestructive Evaluation (IV)" (S. S. Udpa, T. Takagi, J. Pávó, and R. Albanese, Eds.), p. 204. IOS Press, Amsterdam, 2000.
143. G. Simone and F. C. Morabito, in "Electromagnetic Nondestructive Evaluation (IV)" (S. S. Udpa, T. Takagi, J. Pavo, and R. Albanese, Eds.), p. 196. IOS Press, Amsterdam, 2000.
144. G. Simone and F. C. Morabito, in "Electromagnetic Nondestructive Evaluation (V)" (J. Pávó, G. Vértesy, T. Takagi, and S. S. Udpa, Eds.), p. 317. IOS Press, Amsterdam, 2001.
145. A. Gasparics, Cs. S. Daróczi, S. Calcagno, V. Mollo, R. Albanese, and J. Pávó, in "Electromagnetic Nondestructive Evaluation (IV)" (S. S. Udpa, T. Takagi, J. Pávó, and R. Albanese, Eds.), p. 227. IOS Press, Amsterdam, 2000.
146. R. Albanese, S. Calcagno, E. Coccorese, V. Mollo, E. Morabito, F. C. Morabito, G. Reitano, M. Versaci, A. Gasparics, and J. Pávó, in "Non-Linear Electromagnetic System" (P. Di Barba and A. Savini, Eds.), p. 103. IOS Press, Amsterdam, 2000.
147. P. Novotny, M. Morozov, and G. Vertesy, in "Electromagnetic Nondestructive Evaluation (III)" (D. Lesselier and A. Razek, Eds.), p. 26. IOS Press, Amsterdam, 1999.
148. Cs. S. Daróczi, J. Szöllösy, G. Vértesy, J. Pávó, and K. Miya, in "Studies in Applied Electromagnetics and Mechanics 8, Nondestructive Testing of Materials" (R. Collins, W. D. Dover, J. R. Bowler, and K. Miya, Eds.), p. 75. IOS Press, Amsterdam, 1995.
149. Cs. S. Daróczi, G. Vértesy, J. Szöllösy, J. Pávó, and K. Miya, in "Studies in Applied Electromagnetics and Mechanics 10, Nonlinear Electromagnetic Systems" (A. J. Moses and A. Basak, Eds.), p. 748. IOS Press, Amsterdam, 1996.
150. S. Fiori and R. Rossi, *Int. J. of Neural Systems* 13, 273 (2003).
151. G. Vértesy and A. Gasparics, *Mat. Sci. Forum* 414, 343 (2003).
152. T. Takagi and H. Fukutomi, in "Electromagnetic Nondestructive Evaluation (IV)" (S. S. Udpa, T. Takagi, J. Pávó, and R. Albanese, Eds.), p. 235. IOS Press, Amsterdam, 2000.
153. A. Gasparics, G. Vértesy, I. Sebestyén, D. Roger, and T. Takagi, in "Electromagnetic Nondestructive Evaluation (V)" (J. Pávó, G. Vértesy, T. Takagi, and S. S. Udpa, Eds.), p. 317. IOS Press, Amstredam, 2001.
154. T. Takagi and K. Miya, *J. of Japan Society of Applied Electromagnetics and Mechanics* 8, 121 (2000).
155. M. Morozov, G. Rubinacci, A. Tamburino, S. Ventre, and F. Villone, "Proc. 8th Int. Workshop on Electromagnetic Nondestructive Evaluation," Saarbrücken, Germany, 2002.
156. M. Morozov, G. Rubinacci, A. Tamburino, S. Ventre, and F. Villone, in "Electromagnetic Nondestructive Evaluation (VIII)" (T. Sollier, D. Prémel, and D. Lesselier, Eds.), p. 207. IOS Press, Amsterdam, 2004.
157. M. Morozov, G. Rubinacci, A. Tamburino, S. Ventre, and F. Villone, "Proc. 10th Int. Workshop on Electromagnetic Nondestructive Evaluation," East Lansing, Michigan, USA, 2004.
158. A. Gasparics and G. Vértesy, "Proc. Eurosensors XVII. Conf.," Guimaraes, Portugal, 2003.

159. K. Ara, N. Ebine, and N. Nakajima, *J. Pressure Vessel Tech., Trans. ASME* 118, 447 (1996).
160. K. Yamada, S. Shoji, K. Yamaguchi, Y. Tanaka, and R. Grössinger, in "Non-Linear Electromagnetic Systems" (V. Kos and J. Sievert, Eds.), p. 153. IOS Press, Amsterdam, 1997.
161. H. Weinstock, *IEEE Trans. Mag.* 27, 3231 (1991).
162. A. Cochran, J. Macfarlane, L. Morgan, J. Kuznik, R. Weston, L. Hao, R. Bowman, and G. Donaldson, *IEEE Trans. Appl. Supercond.* 4, 128 (1994).
163. S. Shoji, K. Yamada, Y. Tanaka, Y. Uno, Y. Takeda, S. Toyooka, and Y. Isobe, in "Electromagnetic Nondestructive Evaluation (III)" (D. Lesselier and A. Razek, Eds.), p. 129. IOS Press, Amsterdam, 1999.
164. T. Chady, M. Enokizono, T. Todaka, Y. Tsuchida, and R. Sikora, *IEEE Trans. Magn.* 36, 2788 (2000).
165. M. Uesaka, A. Gilanyi, T. Sukegawa, K. Miya, K. Yamada, S. Toyooka, N. Kasai, A. Chiba, S. Takahashi, K. Morishita, K. Ara, N. Ebine, and Y. Isobe, in "Electromagnetic Nondestructive Evaluation (II)" (R. Albanese, G. Rubinacci, T. Takagi, and S. S. Udpa, Eds.), p. 39. IOS Press, Amsterdam, 1998.
166. S. Men, C. Resagk, M. Ziolkowski, M. Kuilekov, and H. Brauer, *Meas. Sci. Technol.* 15, 1323 (2004).